

AD 674403



A PHOTOELASTIC INVESTIGATION OF  
DEEP SUBMERGENCE WINDOWS

Robert Winter  
Herbert Becker

Technical Report No. ARA 315-7  
May 1966

SESSION for	
FSTI	WHITE SECTION <input checked="" type="checkbox"/>
DC	GRAY SECTION <input checked="" type="checkbox"/>
UNANNOUNCED	
JUSTIFIED	
BY	
DISTRIBUTION AVAILABILITY CODES	
CLASS.	AVAIL. and or SPECIAL

Prepared For  
Contract No. NObs-94102  
Bureau of Ships  
Department of the Navy  
Washington, D. C. 20360

ALLIED RESEARCH ASSOCIATES, INC.  
1000 N. 17th St., Suite 100, Arlington, VA 22209

Best Available Copy

**Best  
Available  
Copy**

## SUMMARY

Photoelastic investigations were conducted to determine stresses in  $45^\circ$  seat angle conical frustum plastic windows with diameter/thickness ( $d/h$ ) ratios from 0.5 to 2.5 to embrace the range of current design (on Aluminant, Trieste, and Alvin vehicles,  $d/h = 0.54$ ,  $0.67$ , and  $1.43$  respectively). The results indicate that a window with  $d/h$  less than 1 may be used without significant tensile stresses occurring on the inner face. The effect of seat angle/window angle mismatch was found to have relatively little effect upon stress levels near the cone axis, although local concentrations at the periphery of the inner face were strongly affected.

An important aspect of the study was the tentative identification of the physical nature of the window behavior as a conical sector of a pressurized hollow sphere interacting with a lens shaped cap.

## TABLE OF CONTENTS

	<u>Page</u>
SUMMARY	ii
LIST OF SYMBOLS	v
I. INTRODUCTION	1
A. Scope of General Project	1
B. Status of Data on Window/Shell Interaction	1
C. Scope of Current Investigation	4
D. Acknowledgement	5
II. THEORY	6
A. Introduction	6
B. Photoelastic Background	6
C. Behavior of a Sphere Sector	8
1. Introduction	8
2. Sphere Theory	9
III. EXPERIMENTAL PROCEDURE	11
A. Introduction	11
B. Model Geometries	11
C. Stress Freezing Procedure	11
D. Pressurization Apparatus	14
E. Data Processing	17
F. Separation of Principal Stresses	17
IV. DATA ANALYSIS	22
A. Introduction	22
B. Effect of d/h	22
1. Introduction	22
2. Fringe Data	22
3. Isoclinic Data	24
4. Comparison of Fringe Data with Hollow Sphere Theory	24
5. Maximum Shear Stresses	27
6. Normal Stresses on Centerline	31
7. Seat Angle Mismatch	31

TABLE OF CONTENTS (Continued)

IV	DATA ANALYSIS (Continued)	
	C. Modified Windows	35
	1. Introduction	35
	2. Spherical Small Face	35
	3. Modified Seat Angle	39
	D. Effect of Pressure Level	41
V.	CONCLUSIONS	45
VI.	RECOMMENDATIONS	47
	A. Introduction	47
	B. Improved Designs	47
	C. Long Duration and Cyclical Loadings	47
	D. Seat Angle	47
VII.	REFERENCES	48

## LIST OF SYMBOLS

$a$	Inner radius of sphere, in.
$b$	Outer radius of sphere, in.
$D$	Diameter of large face, in.
$d$	Diameter of small face, in.
$f$	Material fringe value, psi-in/fringe
$h$	Thickness of window, in.
$n$	Fringe order
$P$	Load, pounds
$p$	Pressure, psig
$R$	Radial spherical coordinate, in.
$r, \theta, z$	Cylindrical coordinates: (radial, circumferential, and axial), in., rad. in.
$t$	Thickness of slice, in.
$\alpha$	Geometric parameter
$\sigma_R, \sigma_T$	Stresses in spherical coordinates: radial and tangential, psi
$\sigma_r, \sigma_\theta, \sigma_z$	Stresses in cylindrical coordinates: radial, circumferential, and axial, psi
$\sigma_1, \sigma_2$	Principal stresses at a point in a slice, psi
$\tau_{\max}$	Maximum shear stress at a point in a slice, psi
$\tau_{rz}$	Shear stress in r-z plane, psi
$\phi$	Isoclinic angle above horizontal, radians or degrees

## I. INTRODUCTION

### A. Scope of General Project

Piccard reported results of tests on methyl methacrylate windows showing that window strength decreased with increasing face diameter for a given thickness (Ref. 1). However, the scatter in the reported data is large, and the basis for judging the window strength was not clear.

Since Piccard reported the results of his studies on conical frustum plastic windows no further data have appeared in the literature either to define the stresses in windows, or to show how window strength is related to stresses and basic material properties. It is the purpose of this investigation to seek answers to those questions in order to aid establishment of scientific procedures for window design for all submergence depths.

This section of the report discusses the background on window behavior developed by ARA to date and the relation to optimum sphere design, and describes the general character of the current project which was devoted to window stress determination.

### B. Status of Data on Window/Shell Interaction

The basic window geometry is shown in Fig. 1. The current state of information relating to window/shell interaction was discussed in Refs. 2 and 3. For a typical window (Fig. 1), the behavior may be seen in Fig. 2 which depicts the membrane stress concentration at the window penetration in an unreinforced spherical shell under external hydrostatic pressure. The stress concentration is relative to the membrane stress in a simple unpenetrated sphere and is given as a function of window seat angle and Young's modulus ratio of shell to window. The following tentative explanation was offered for the results observed in that figure.

Apparently a rigid window with a small chamfer angle acts as a continuation of the shell. This effect was observed on hatches with  $15^{\circ}$  seat angles (Ref. 3). As the seat angle increases, the rigidity of the window may be too great to permit a simple pressure loading of the sloped seat. Apparently, the external pressure

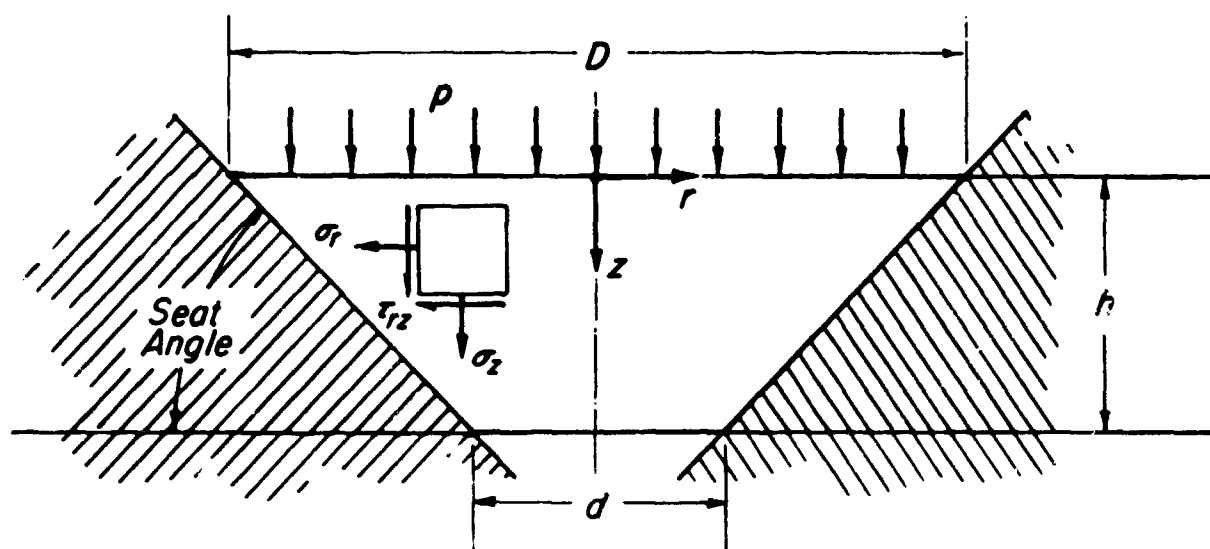
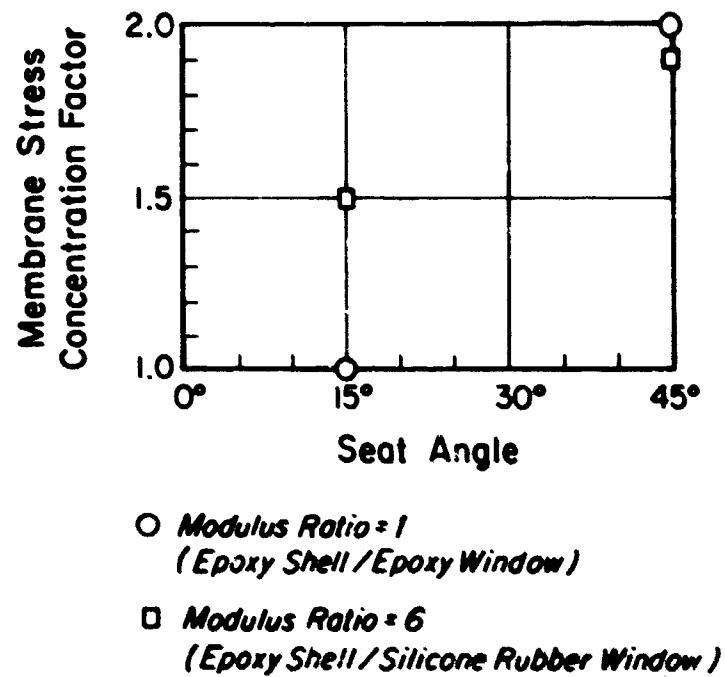
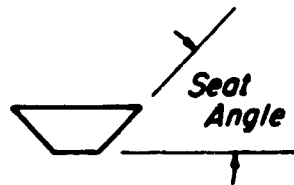


Figure 1 Cross-section of a deep submergence window.





**Figure 2** Membrane stress concentration around a conical window in an unreinforced spherical shell as a function of seat angle and modulus ratio.

force would tend to push a stiff window radially inward, thereby generating shearing forces on the circumference of the seat which would lead to large bending moments in the shell. The flexible window, on the other hand, seems to be unable to support the structural continuity of the shell at any chamfer angle. However, at the larger chamfer angles, the adaptability of the more flexible window to the deformed shape of the shell seat allows pressure loading on the shell seat, thereby providing relief to the stress field generated at the hole by the membrane forces in the shell. The stiffer window cannot provide this relieving effect.

As is evident from these results, it is necessary to define more clearly the effect of seat angle and modulus ratio upon the behavior of the shell. The preceding investigations were conducted upon unreinforced shells. Therefore, an additional factor in the analysis of the shell would be the effect of reinforcement.

The data of Ref. 2 on window stresses, which were obtained on epoxy windows in a steel hemisphere seat, reveal a shear stress distribution with a maximum inside the window approximately one bottom face radius upward from the bottom face into the interior. In addition, there are stress concentrations on the boundary. The magnitude of the maximum shearing stress was found to be appreciably less than the pressure. Furthermore, it was evident from that study that the relatively low applied pressure (1,000 psi) could not generate a stress high enough in magnitude to initiate failure of the window.

Since the modulus ratio for the steel/plexiglas combination is approximately 60, it is reasonable to suppose that the plexiglas had sufficient flexibility to adjust to deformations of the shell which may have been generated during loading. This probably would not be the case with a stiff window such as solid glass, for which the modulus ratio could be as low as 3. Therefore, the problem areas in connection with the design of the window involve the same parameters (modulus ratio, seat angle, and the nature of the reinforcement) as those affecting the design of the shell.

### C. Scope of Current Investigation

Before the design optimization of a plexiglas window is attempted, a strength evaluation should be made to establish scientifically (in contrast to the imprecise parameters of Ref. 1) the relation between maximum pressure which the window can support and the mechanical properties of the window material. The seat angle, internal aperture diameter and thickness would be the principal geometric factors to be considered. Additional factors such as mismatch of shell seat and window chamfer could be important.

The initial step in the process is the systematic elastic analysis of the window stresses. The project described in this report was addressed to that purpose on windows with  $45^{\circ}$  seat angles ( $90^{\circ}$  cone angles).

D. Acknowledgement

The authors wish to thank Mr. Richard Lederman for his capable assistance with the experiments and the calculations.

## II. THEORY

### A. Introduction

The current investigation utilized photoelastic data to determine boundary stresses, and to separate the principal stresses on the centerline of a window. In addition, sphere theory was used for comparison with the observed experimental results. This section presents the background for these procedures, application of the results of which are described in subsequent sections.

### B. Photoelastic Background

In the photoelastic analysis thin flat slices of constant thickness were cut from three dimensional stress frozen models. The fringe patterns revealed the stresses lying in the plane of the slice. For these window models, the most useful single slice was in a vertical plane passing through the centerline, since it revealed the character of the stresses throughout the cross section of the symmetrical model. This type of slice was cut from all the models in this study.

At each point in a thin slice taken from a model, the fringe order is related to the maximum shear stress (1/2 the difference of the principal normal stresses) acting in the plane of the slice

$$nf/t = 2\tau_{\max} = \sigma_1 - \sigma_2 \quad (1)$$

It can be seen that when the fringe order is zero, the shear stress vanishes and the principal stresses are equal (or possibly zero). At a pressurized surface, where the value of the stress perpendicular to the edge is known, the tangential normal stress can be found directly from Eq. (1).

The fringe value depends on the wavelength of the light used in viewing the fringe pattern (the same 5461 Angstrom filter was used in all cases) and was measured for each model by calibrated disks loaded in compression across a diameter. The principal stress difference at the center of such a disk is  $8P/\pi Dt$ , where  $P$  is the compressive load and  $D$  is the diameter (Ref. 4). Eq. (1) then gives the calibration formula

$$f = 8P/\pi Dn \quad (2)$$

which allows the determination of the material fringe values.

The two principal stresses at a point,  $\sigma_1$  and  $\sigma_2$ , while mutually perpendicular, are generally oriented at an angle to the horizontal. This angle varies for different points in the slice. The angle of inclination of the principal stresses through the slice is revealed by an isoclinic curve which connects all points having the same angle. A complete set of photoelastic data for a slice would be an isochromatic fringe pattern together with isoclinics for various angles of inclination. The isoclinics are generally needed to permit separation of principal stresses in a slice.

The internal stress distribution should be symmetric about the cone axis in a cylindrical coordinate system. Therefore,  $\sigma_r$ ,  $\sigma_\theta$ ,  $\sigma_z$ , and  $\tau_{rz}$  will be independent of the circumferential position  $\theta$ , and the other shear stresses must vanish.

Consequently, at the centerline of the slice the fringe order can be directly related to the stresses  $\sigma_r$  and  $\sigma_z$  lying in the plane of the slice (see Fig. 1). Since on the  $z$  axis,  $\sigma_r = \sigma_\theta$  and  $\tau_{rz} = 0$ , the complete state of stress is determined along the centerline by  $\sigma_r$  and  $\sigma_z$ .

The isochromatic and isoclinic data were used to determine the stresses along the centerline of the slice. The analysis follows from the theory of elasticity and the condition of symmetry along the centerline. The distribution of axial stress between the known values of  $-p$  at  $z=0$  and  $0$  at  $z=h$  is found first. The pertinent equation of equilibrium in cylindrical coordinates is

$$\frac{\partial \sigma_z}{\partial z} + \frac{\partial \tau_{rz}}{\partial r} + \frac{\tau_{rz}}{r} = \frac{\partial \sigma_z}{\partial z} + \frac{1}{r} \frac{\partial}{\partial r} (r \tau_{rz}) = 0 \quad (3)$$

where the stresses and coordinate directions are defined as in Fig. 1. Integrating Eq. (3), the variation of  $\sigma_z$  along the  $z$  axis is

$$\sigma_z(z) \Big|_{r=0} = \sigma_{z0} - \int_{z_0}^z \left[ \frac{1}{r} \frac{\partial}{\partial r} (r \tau_{rz}) \right]_{r=0} dz \quad (4)$$

The derivative  $\frac{\partial}{\partial r} (r \tau_{rz})$  can be found from the Mohr's circle relation

$$\tau_{rz} = \frac{1}{2} (\sigma_1 - \sigma_2) \sin 2\phi$$

which holds everywhere in the body. The stresses  $\sigma_1$  and  $\sigma_2$  are the principal stresses at any point and  $\phi$  is the angle of inclination of these stresses with respect to the horizontal, equal to the isoclinic angle at that point. In terms of the photoelastic data, this becomes, using Eq. (1),

$$\tau_{rz} = \frac{nf}{2t} \sin 2\phi$$

and

$$\frac{\partial}{\partial r} (r\tau_{rz}) = \frac{f}{2t} \left[ \left( r \frac{\partial n}{\partial r} + n \right) \sin 2\phi + 2nr \frac{\partial \phi}{\partial r} \cos 2\phi \right]$$

On the centerline,  $r=0$ ,  $\phi=0$ , and

$$\left[ \frac{1}{r} \frac{\partial}{\partial r} (r\tau_{rz}) \right]_{r=0} = \frac{f}{t} \left[ n \frac{\partial \phi}{\partial r} \right]_{r=0}$$

Eq. (4) becomes, starting with  $\sigma_{z_0} = -p$  at  $z_0 = 0$ ,

$$\left[ \sigma_z(z) \right]_{r=0} = -p - \frac{f}{t} \int_0^z \left[ n \frac{\partial \phi}{\partial r} \right]_{r=0} dz \quad (5)$$

where  $n$  is taken positive when  $\sigma_r > \sigma_z$ . Using the isochromatic and isoclinic fringe data with Eq. (5),  $\sigma_z$  can be found along the centerline as it varies from  $-p$  at the large face to zero at the small face. The stress  $\sigma_r$  is then found from

$$\sigma_r = \sigma_z + (nf/t) \quad (6)$$

### C. Behavior of a Sphere Sector

#### 1. Introduction

In the absence of a theory to predict the elastic stress field in a conical frustum window, a comparison was made with the stresses in a conical sector of a hollow sphere to determine how the fringe pattern data of the two would be related. The physical behavior of a frustum window should have some similarity with that of a sphere sector, except for the possible influence of friction. If a hollow sphere were to be externally pressurized a conical sector would remain a cone because of symmetry. The sector would move inward within the confines of the cone boundary in the same way as a flexible window in a comparatively rigid seat.

This viewpoint prompted the investigation of sphere sectors of inner and outer radii  $a$  and  $b$  respectively (Fig. 3).

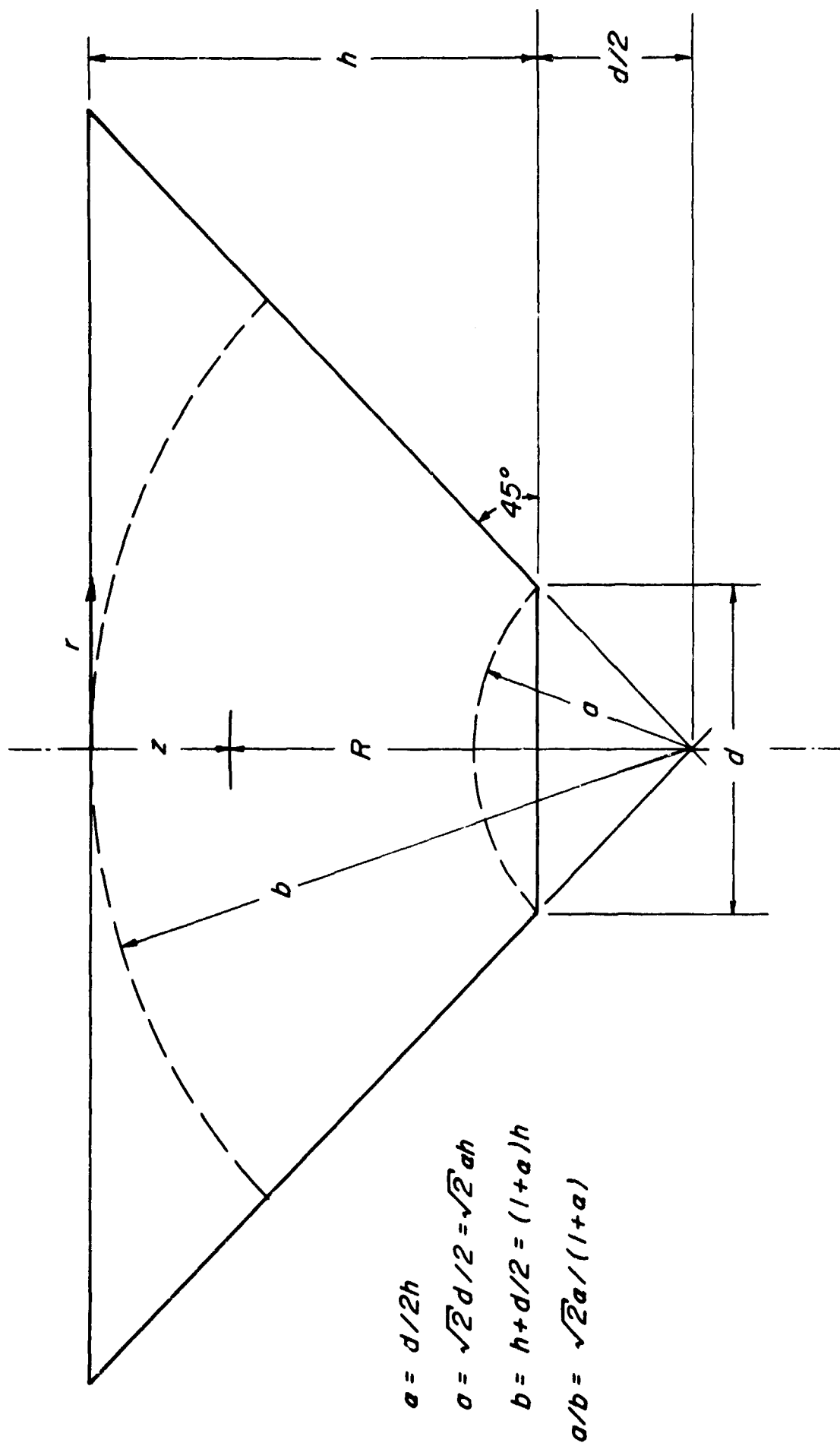


Figure 3 Segment of a hollow sphere superimposed on the window.

## 2. Sphere Theory

The tangential, radial, and difference stresses in an externally pressurized sphere are, in the spherical coordinate system used in Ref. 5:

$$\sigma_T = \frac{pb^3 (R^3 + 0.5a^3)}{R^3 (b^3 - a^3)}$$

$$\sigma_R = \frac{pb^3 (R^3 - a^3)}{R^3 (b^3 - a^3)}$$

$$\sigma_T - \sigma_R = nf/t = \frac{3pa^3b^3}{2R^3(b^3 - a^3)}$$

From Fig. 3,  $a = (\sqrt{2}/2)d$  and  $b = d/2 + h$ . If  $a$  is chosen such that  $a = d/2h$ , then  $d = 2ah$ ,  $a = \sqrt{2}ah$ ,  $b = (1+a)h$ ,  $a/b = \sqrt{2}a/(1+a)$  and

$$\frac{\sigma_T - \sigma_R}{p} = \frac{nf}{pt} = \frac{(3\sqrt{2}) (ah/R)^3}{1 - 2^{3/2} a^3 / (1+a)^3} \quad (7)$$

However, the tangential and radial stresses in the spherical coordinates of Ref. 4 correspond respectively to the radial and axial stresses along the centerline in the cylindrical coordinate system used here (Fig. 3). On the  $z$  axis, then,  $R/h = 1 + a - z/h$  and Eq. (7) becomes

$$\frac{\sigma_r - \sigma_z}{p} = \frac{nf}{pt} = \frac{3\sqrt{2} a^3}{(1+a - z/h)^3 [1 - 2^{3/2} a^3 / (1+a)^3]} \quad (8)$$



### III. EXPERIMENTAL PROCEDURE

#### A. Introduction

Six  $d/h$  values were selected for the photoelastic studies of window stresses. All models were stress frozen in apparatus specially designed for this project. Measurements were made and photographs were taken of the fringe patterns and isoclinics in the central slices of each model. The boundary stresses and maximum shear stresses were determined for all slices, and in two cases ( $d/h = 0.75$  and  $1.5$ ) the principal stresses were separated along the cone axis.

#### B. Model Geometries

Ten models were machined covering the range of  $d/h$  values from 0.5 to 2.5 (Table 1). The models had a nominal seat angle of  $45^\circ$  (Fig. 1), a nominal large face diameter  $D$  of 2.5 inches, and were machined with smooth surfaces (32 rms). As each model was machined, a calibration disk was made from material in the same location in the epoxy stock. This disk was used later to determine the material fringe value  $f$  of the model. A typical window model and calibration disk are shown in Fig. 4. The dimensions of all models were measured before testing.

#### C. Stress Freezing Procedure

The internal stress fields of the scaled three dimensional models were obtained using the stress freezing photoelastic technique which was successfully employed in many previous investigations for the Navy Department. In this procedure, models are heated above a critical temperature, the load is applied, and upon returning to room temperature, the photoelastic fringe patterns resulting from the applied loads are locked or "frozen" into the material. Thin slices are then cut from the three dimensional model so that the photoelastic fringe patterns can be read, thereby revealing the stresses in the plane of the slice which can be related to the applied pressure.

Specifically in this study, the fixture with the enclosed model was placed in the oven and brought to a uniform temperature of  $300^\circ\text{F}$ . After setting the pressure on the large face of the model at the desired value, the temperature was lowered at the constant rate of  $5^\circ\text{F}$  per hour. This slow rate was chosen in order to maintain a nearly uniform temperature distribution in the model thus minimizing thermal stresses. A check performed on a dummy model with a thermocouple imbedded in

Table 1

## Model Data

Model No.	D inches	d inches	h inches	d/h	Calculated seat angle (+1')	Seat angle mismatch <sup>a</sup> (+2')	Calculated initial gap inches	P psi	f psi/fringe/inch
1	2.495	0.499	1.006	0.495	45°14'	+3'	0.0012(L) <sup>c</sup>	0	1.34
2	2.498	0.500	1.010	0.495	45°19'	+8'	0.0023(L)	10	1.34
3	2.489	0.500	1.003	0.498	45°14'	+3'	0.0012(L)	40	1.36
4	2.486	0.683	0.909	0.751	45°14'	+3'	0.0011(L)	40	1.43
5	2.510 <sup>b</sup>	0.830	0.835	0.995	-- <sup>b</sup>	-- <sup>b</sup>	-- <sup>b</sup>	40	1.44
6	2.492	1.069	0.713	1.50	45°3'	-8'	0.0023(S)	40	1.38
7	2.493	1.248	0.625	1.95	45°7'	-4'	0.0010(S)	40	1.37
8	2.491	1.385	0.556	2.49	45°8'	-3'	0.0007(S)	40	1.42
9	2.492	0.665	0.909	0.732	44°48'	-23'	0.0086(S)	40	1.36
10 <sup>d</sup>	2.495	0.694	0.906	0.765	45°18'	+7'	0.0026(L)	40	1.42

<sup>a</sup>Seat angle of steel fixture was 45°11' ( $\pm 1'$ ).

<sup>b</sup>D measurement in error, preventing calculation of angles.

<sup>c</sup>(L) indicates gap at edge of large face. (S) at edge of small face.

<sup>d</sup>Spherical surface at small face.

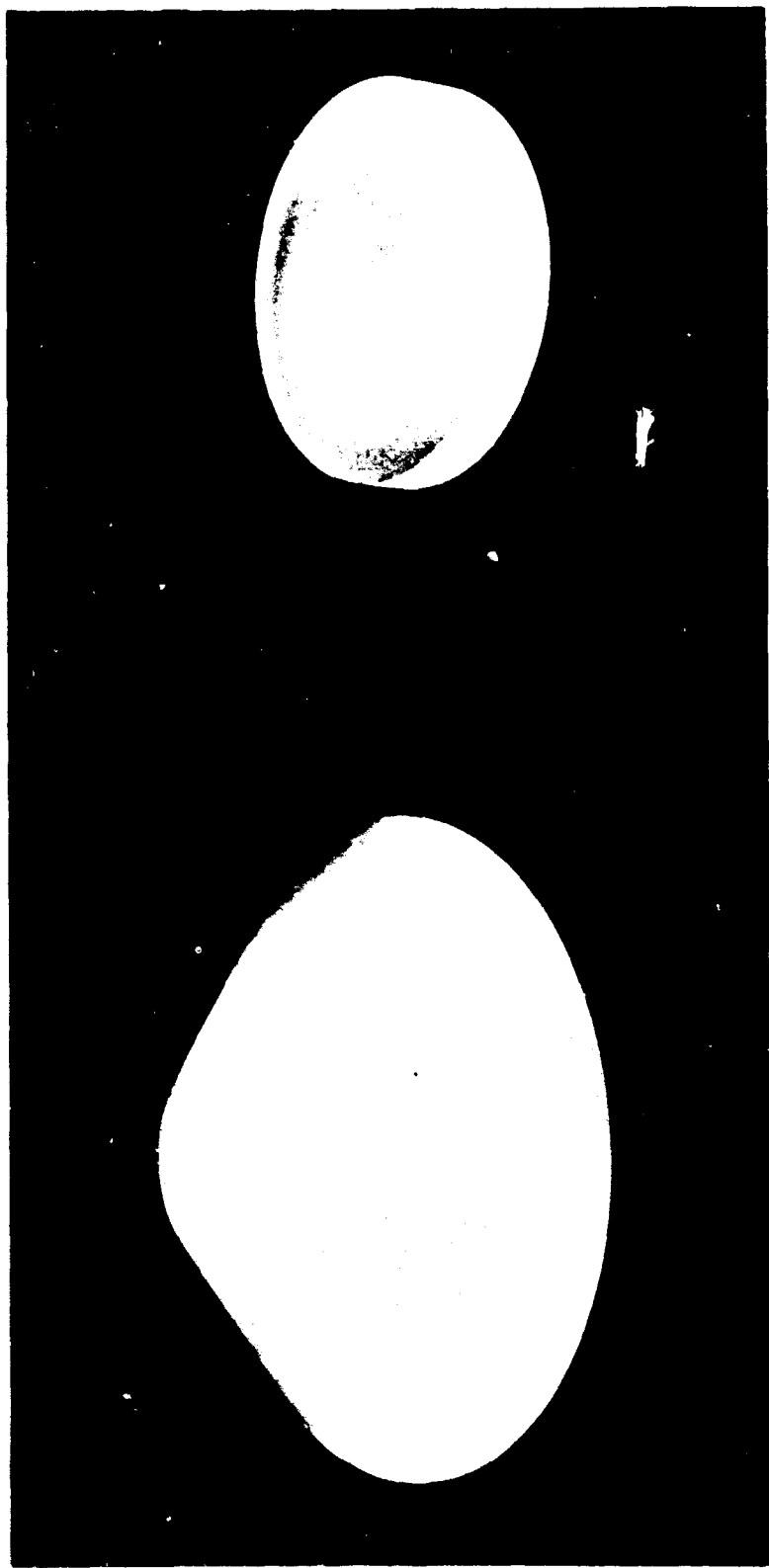


Figure 4 Typical window model and its calibration disk.

the center indicated that the temperature was sufficiently uniform to be always within one degree of the ambient oven temperature throughout the stress freezing range.

Each calibration disk was stress frozen at the same time as the associated window model. By loading the disk in compression across a diameter, a known stress state was induced at the center and by measuring the fringe order, the material fringe value of the model was found (Eq. (2), above). This constant was used later to convert fringe order into stress.

Epoxy was chosen as the model material because it has a high fringe sensitivity to applied stress ( $f = 1.4$  typically). This allowed a low pressure loading to produce a fringe pattern of sufficiently high order to permit accurate stress determination.

#### D. Pressurization Apparatus

The experiments were designed to expose the window models to conditions representative of deep submergence, but with a minimum of interference from secondary effects such as seat movement. Accordingly, the influence of the flexibility of any surrounding structure, possibly important in the final application, was minimized in this present study by using a heavy seating fixture. The seat/shell structure interaction is discussed in Section I.

The steel seating fixture, shown in Fig. 5, was machined with a conical hole of  $45^\circ$  nominal seat angle and a smooth ( $\pm 2$  rms) surface. The cover of the fixture was provided with holes for a pressurized gas inlet and a pressure gauge tap, and was bolted to the fixture with an O-ring seal between them. The conical surface of each model was coated with a thin layer of GE Viscasil 5000 silicone fluid which sealed the model against the seat during the initial application of gas pressure and provided lubrication. A small hole at the apex of the conical seat insured that the small face was at atmospheric pressure at all times. The heavy steel seat fixture was rigid with respect to the models under the test conditions, the modulus ratio of steel to epoxy at the stress freezing temperature being  $>10^4$ .

Fig. 6 is an overall view of the equipment used, showing the seating fixture and the calibration disk in the loading frame in the oven, the pressure control panel, and the nitrogen gas supply.



Figure 5 The steel seating fixture and cover.

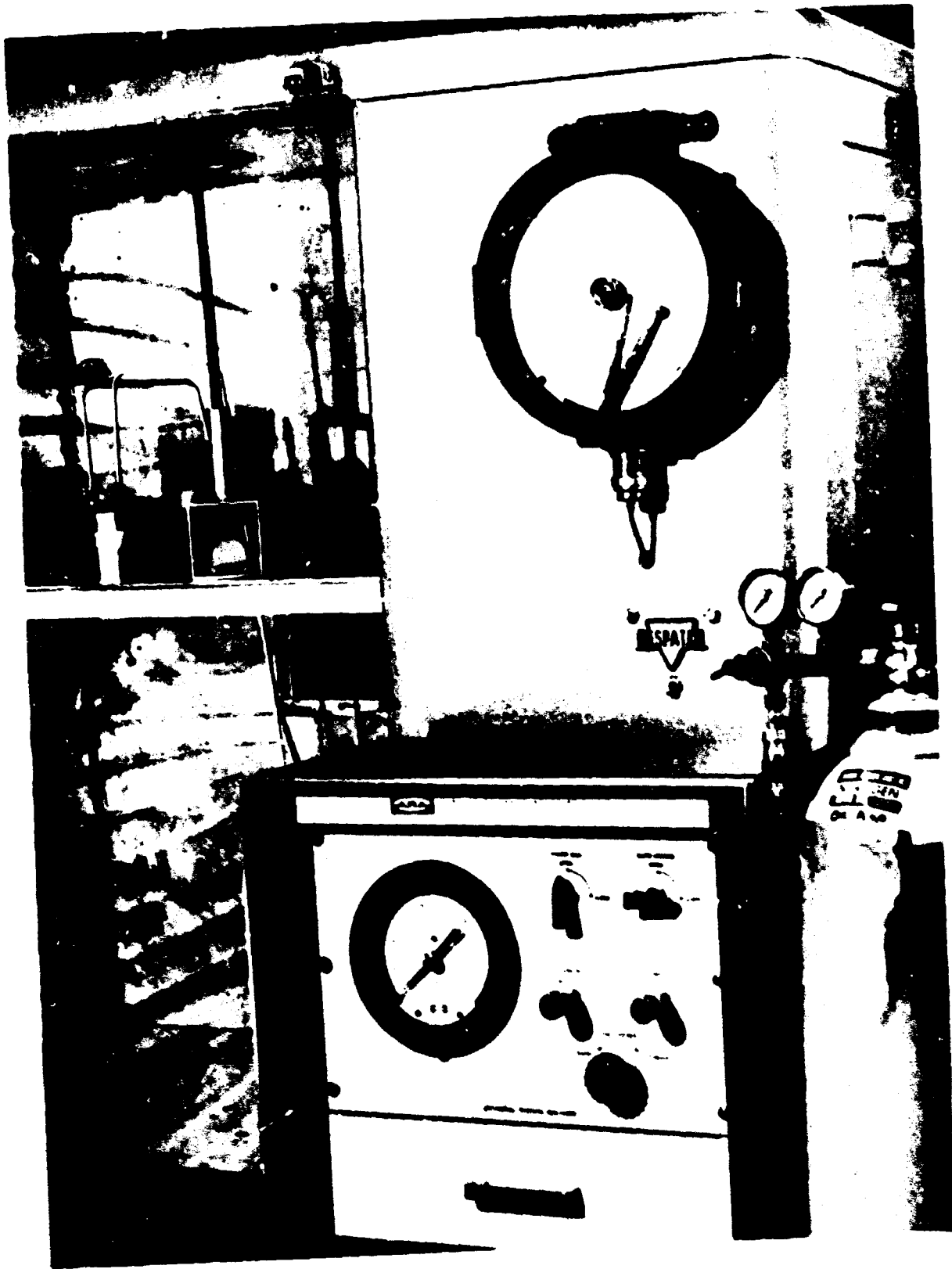


Figure 6 Overall view of the stress freezing equipment.

### E. Data Processing

After cooling, the models were removed from the fixture and placed in the polariscope shown in Fig. 7, where they were checked for evidence of non-symmetric loading by viewing the fringe pattern through the faces. The symmetry of the fringe pattern shown in Fig. 8 is typical of the results achieved with the models tested. The zero order fringe appearing at the center in this view confirmed the validity of the assumption in Section II that  $\sigma_r = \sigma_\theta$  on the centerline. A 1/8 inch thick slice was then cut through the center of each model, as in Fig. 9, and photographs were taken of the isochromatics and isoclinics. The isochromatic fringe photographs were taken through a 5461 Angstrom filter. The fringe orders at certain points in each slice were measured using a Babinet compensator with an accuracy of  $\pm 0.05$  fringe.

### F. Separation of Principal Stresses

The integral of Eq. (5) was evaluated numerically from the data. The fringe pattern and  $0^\circ$ ,  $5^\circ$ , and  $10^\circ$  isoclinic photographs were enlarged to about 12 times actual size. From these enlargements the function  $n(z)$  was found and isoclinic angle trajectories were traced as shown schematically in Fig. 10. At several values of  $z$  the variation of isoclinic angle with radial distance was plotted to determine the local slope  $\partial\phi/\partial r$  on the centerline for use in Eq. (5).



Figure 7 A window model slice in the polariscope.



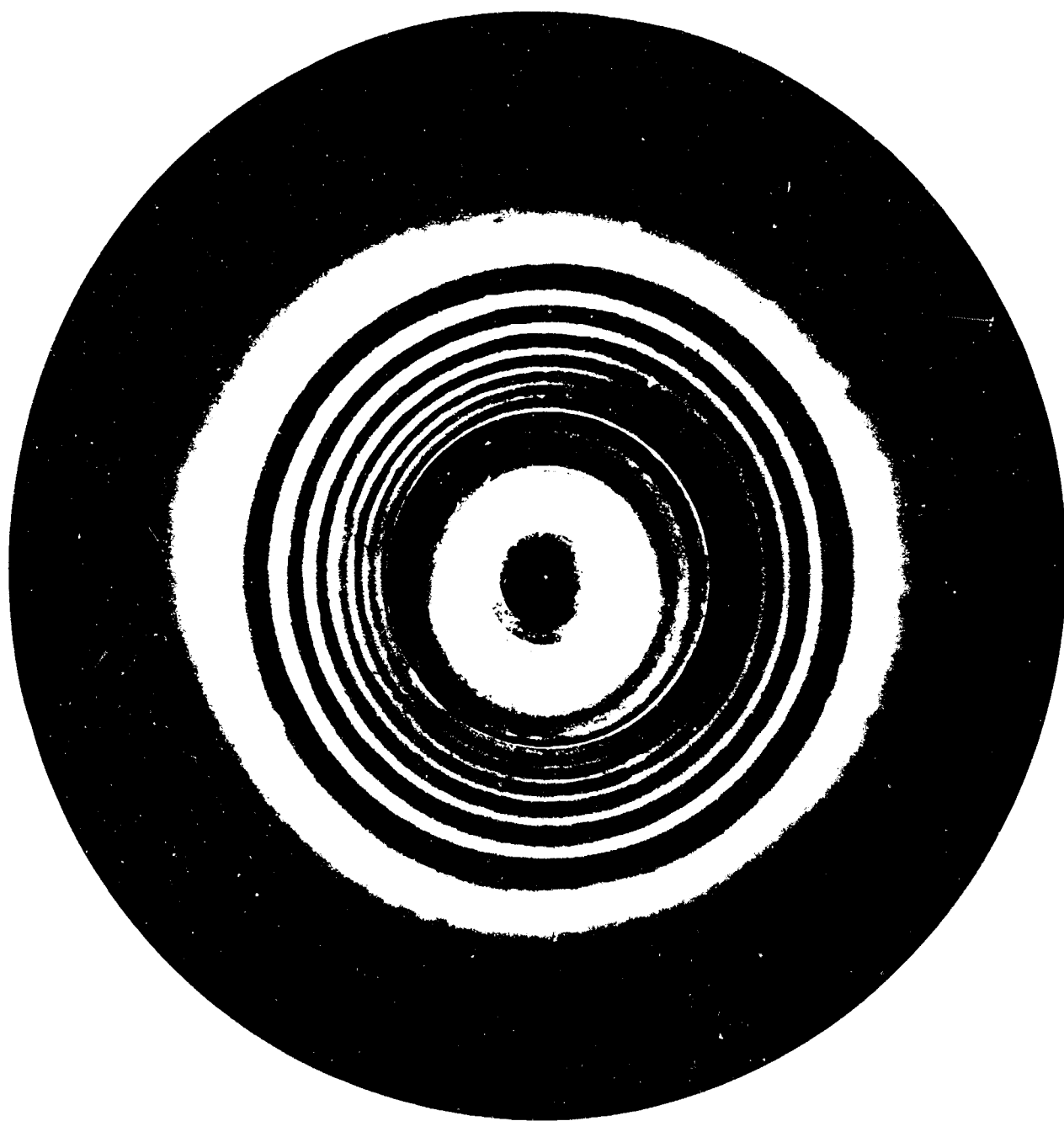


Figure 8 Symmetric fringe pattern of a window model, looking at the small face.

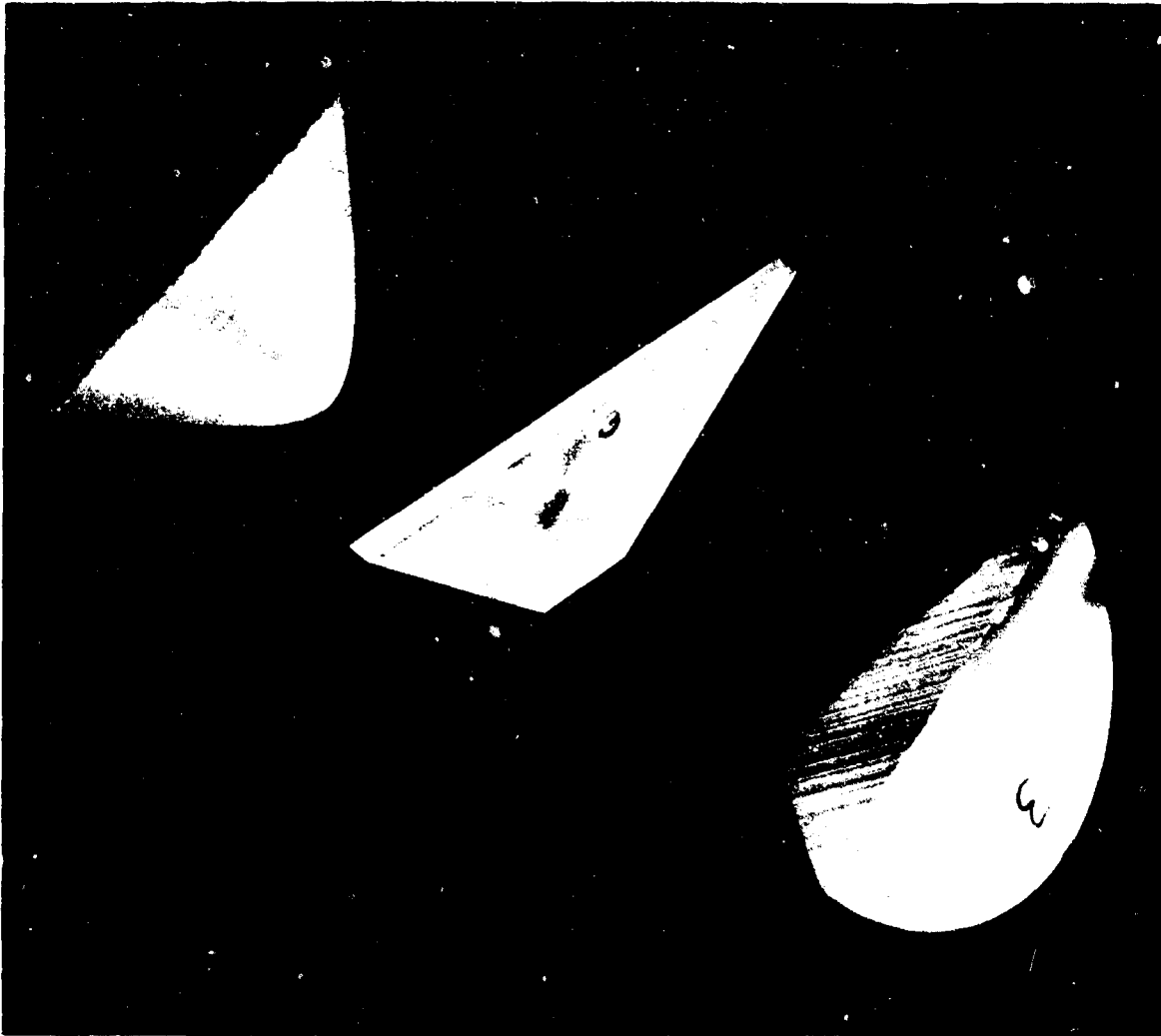


Figure 9 Typical sliced model after stress freezing.

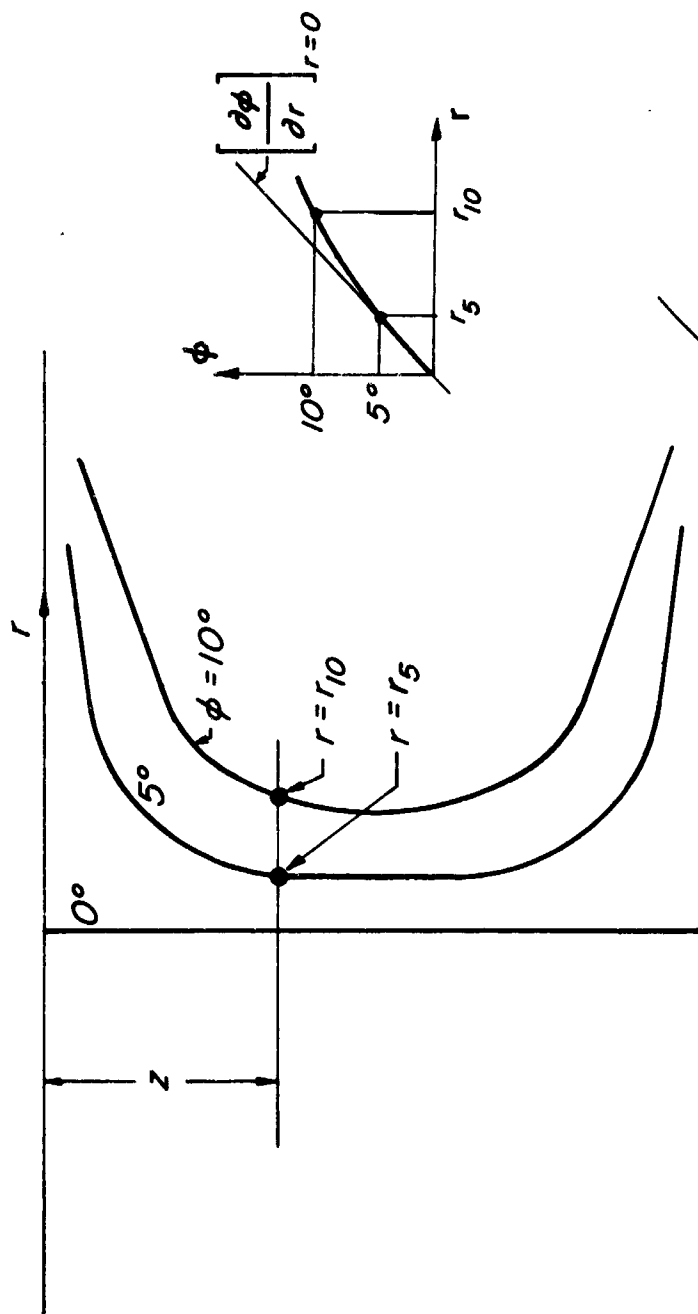


Figure 10 Sketch of isoclinic tracings used in calculation of principal stresses along centerline.

## IV. DATA ANALYSIS

### A. Introduction

The photoelastic data were taken primarily to expose the character of the stresses in the basic window design over the range  $0.5 \leq d/h \leq 2.5$ . This was achieved mainly by examination of the fringe and isoclinic photographs and the stresses calculated from the fringe data. The importance of the initial seat angle mismatch between the model and the seat fixture was also examined.

A second set of data was taken to examine possible ways of modifying the geometry of the windows to reduce stress concentrations, and a few models were studied to determine the effect of pressure level upon the stress distribution.

### B. Effect of $d/h$

#### 1. Introduction

The effect of variations of  $d/h$  on the stresses in the windows was determined from models 3 through 8 (Table 1) with nominal  $d/h$  ratios of 0.5, 0.75, 1.0, 1.5, 2.0, and 2.5, all with an applied pressure of 40 psig. The major effort was on analysis of the data on the centerlines. The principal stresses were determined along this axis for two of the models.

#### 2. Fringe Data

The fringe patterns of the six models are compared in Fig. 11. Accurate measurements of the fringe order were made at the centers of each face and at the fringe concentrations just above the sides of the small faces. Measurements were also made at points of maximum and minimum fringe order on the centerlines.

Fig. 11 indicates that all models had a region of zero fringe order near the large face which varied in size over the  $d/h$  range, being smaller for the higher  $d/h$  ratios. These zero fringe order regions maintained their character regardless of orientation of the unsliced model in the polariscope. Furthermore, all the isoclinics passed through these areas. Therefore, these portions of the windows were under a hydrostatic compression  $\sigma_r = \sigma_\theta = \sigma_z = -p$ ,  $\tau_{rz} = 0$ . This hydrostatic state extended almost uniformly across the upper regions near the large face for  $d/h = 0.5$  and receded into the corners as  $d/h$  increased. Correspondingly, the higher order fringes and shear stresses were confined to the lower regions near the small faces for  $d/h = 0.5$  and spread upward and outward as  $d/h$  increased.

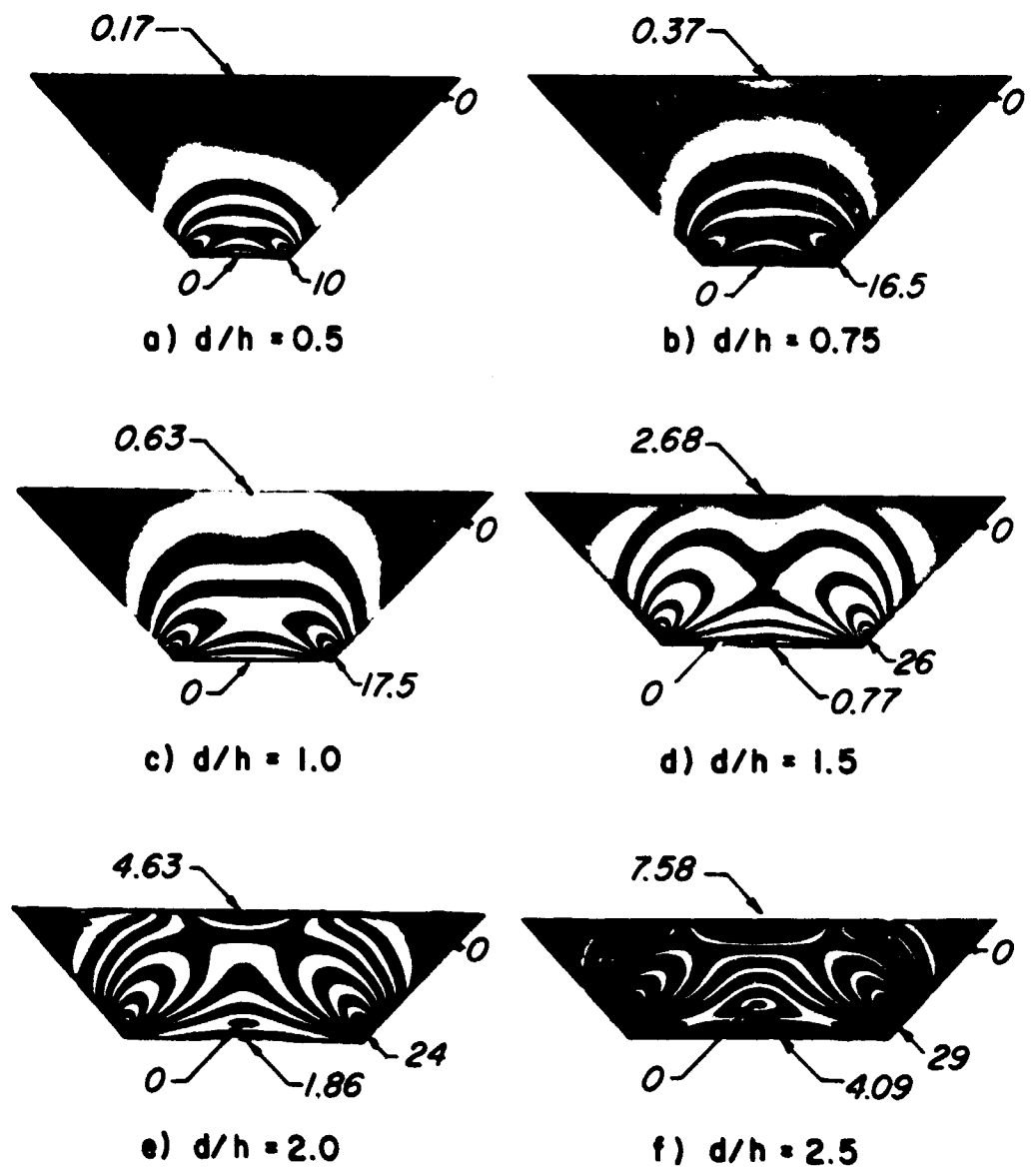


Figure 11 Dark-field fringe patterns from models having various  $d/h$  ratios

Note that the presence of the large face boundary, occurring in a region of hydrostatic stress, did not seem to affect the fringe pattern until  $d/h = 1.5$ . At  $d/h = 2.5$ , the fringe pattern along the centerline was similar to that of a circular plate under combined bending and radial compression, having nearly evenly spaced fringes and the zero order fringe displaced vertically from the horizontal midplane. When viewing the models through the faces, as in Fig. 8, a zero order fringe was observed at the center, confirming the validity of the assumption that  $\sigma_r = \sigma_\theta$  on the centerline.

### 3. Isoclinic Data

The  $0^\circ$ ,  $20^\circ$ , and  $45^\circ$  isoclinics from the six models were selected from the total set for display in Fig. 12. The isoclinics verify the symmetry of loading and indicate that the shear stresses developed along the conical surfaces of the windows. In all cases, the  $0^\circ$  isoclinic was coincident with the centerline so that on this axis the stresses  $\sigma_r$  and  $\sigma_z$  were the principal stresses (which could be expected from symmetry) and the maximum shear stress was at  $45^\circ$  to the horizontal. The  $0^\circ$  isoclinic also appeared along the large and small faces, where the principal stresses were perpendicular and parallel to the pressurized and unloaded surfaces. The  $45^\circ$  isoclinic occurred along the upper portions of the  $45^\circ$  sloping sides indicating that no surface shear forces existed there. On the lower portion of the sides, the isoclinics indicated that surface shears due to friction were present. The surface shear forces covered an increasing proportion of the conical surface as  $d/h$  increased.

### 4. Comparison of Fringe Data with Hollow Sphere Theory

The variation of fringe order along the centerline of each model was compared to the predictions of the hollow sphere theory of Eq. (8). The results show (Fig. 13) that the hollow sphere concept is fundamental to the window behavior for  $d/h \leq 1.0$ . For  $d/h = 0.50$ , there is excellent agreement of theory and experiment over 80% of the centerline, with a severe deviation near the small face since the geometry at that location is far from that of a hollow sphere. There was no such difference between window data and sphere theory near the flat large face because the hydrostatic compression in that region apparently allows the presence of any shaped surface without noticeably changing the stress distribution.

For  $d/h = 0.75$ , the agreement of experiment and sphere theory is reduced but still obvious. Since the flat face was now proportionately wider, the deviatory effects penetrated deeper into the window. Agreement over the remaining 65% of the centerline is still satisfactory.

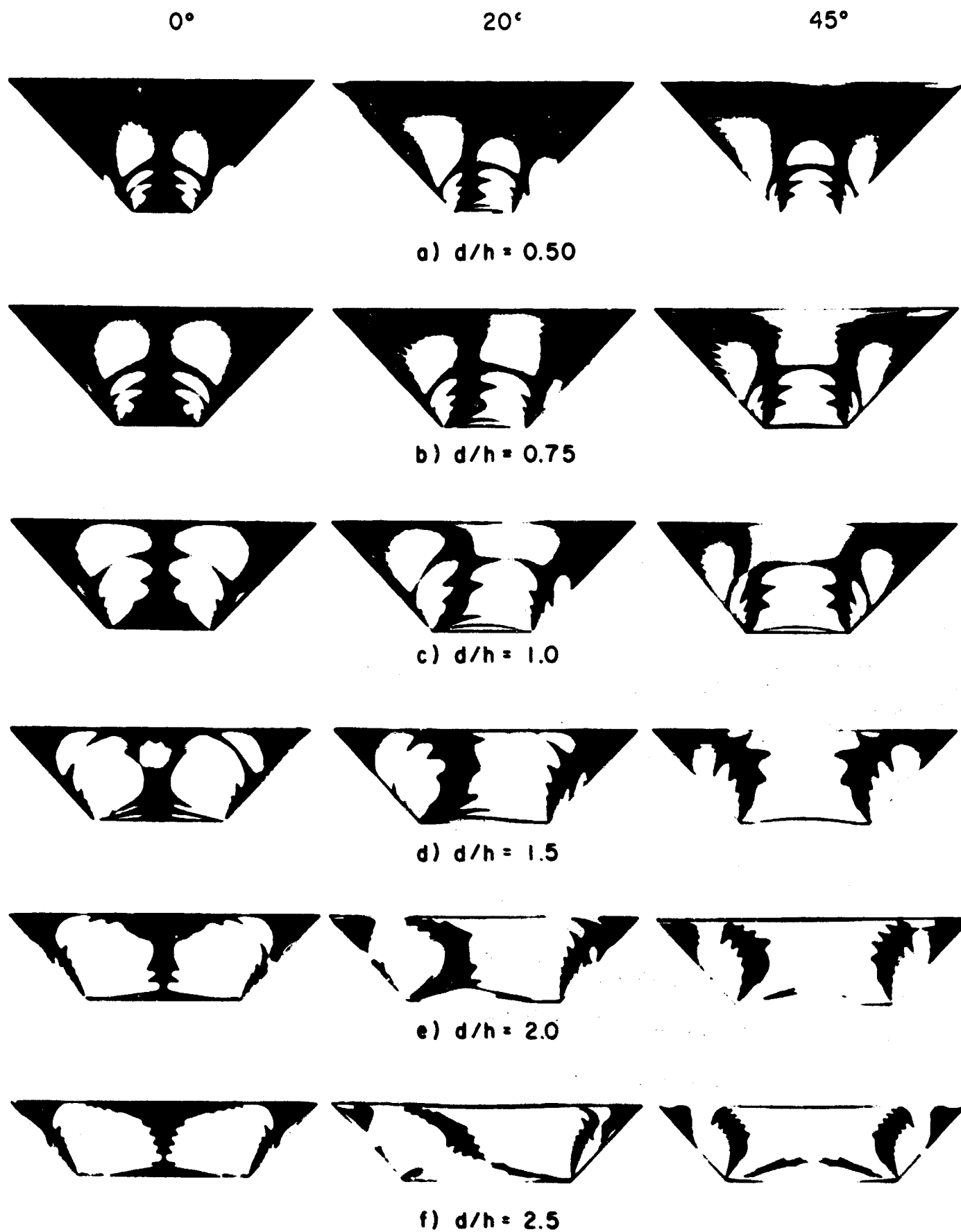


Figure 12    0°, 20°, and 45° isoclinics in window models.

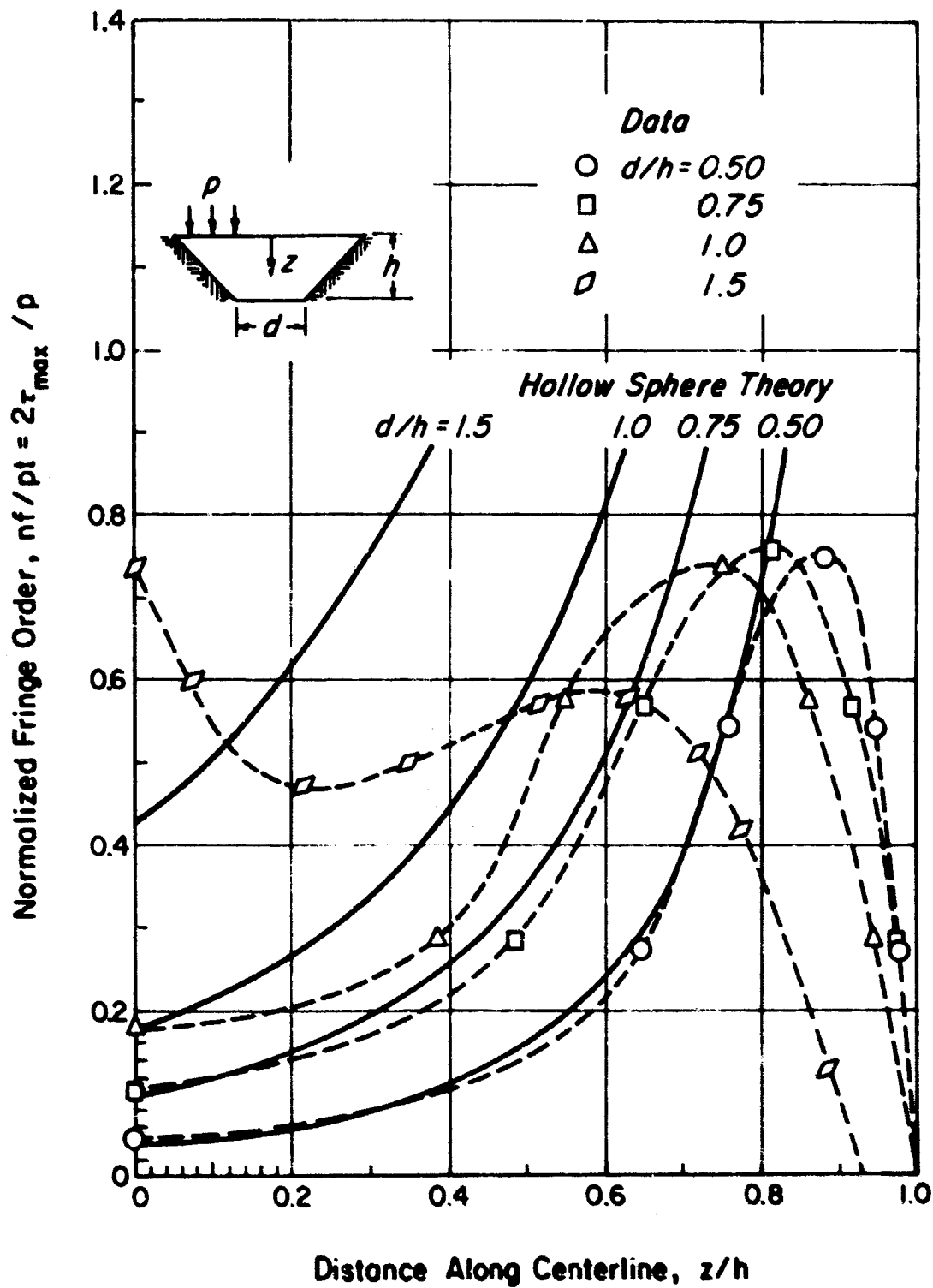


Figure 13 Comparison of fringe data along the centerline with hollow sphere theory.



The data for  $d/h = 1.0$  showed the first serious general departure from the sphere theory. The effect of the flat face had penetrated to half the height of the window, and there was only rough correspondence over the remaining 50%, except for the still excellent agreement at the large face.

For  $d/h$  as large as 1.5, the data in Fig. 13 no longer bear comparison to the simple hollow sphere theory. The hydrostatic stress state no longer covered the large face and the small face was now so large that the window behavior lost all resemblance to that of a segment of a hollow sphere. Evidently, the change from a conical plug to a flat circular plate becomes most marked when  $d/h$  is greater than 1.0.

#### 5. Maximum Shear Stresses

In each model as can be seen in Fig. 11, there was a locus of maximum fringe order and maximum internal shear stress along a semi-elliptical surface terminating at the fringe concentrations appearing on the cones near the small face. For  $d/h = 0.5$  this surface was shallow and it occurred higher in the window as  $d/h$  increased. The maximum shear stress on the centerline, (oriented at  $45^\circ$  to the horizontal) is plotted in Fig. 14 as a function of  $d/h$ . For  $d/h < 1.5$ , this maximum occurred in the interior and varied only slightly in value, as in Fig. 13. When  $d/h = 1.5$ , the maximum shear stress on the centerline shifted to the large face, as the fringe patterns underwent the change to plate action.

The maximum fringe order in each model was developed on the conical surfaces just above the small face, the concentric fringes indicating the presence of concentrated contact forces there. Fig. 15 is an approximately 68X enlargement of a typical corner fringe concentration, from which measurements of the maximum fringe order were made. The curvature of the conical surface prohibited the viewing of the fringe pattern at the actual edge of the model. This is unavoidable in a slice of finite thickness. Fringe order measurements were made as close to the edge as possible and fringe values were extrapolated to the actual edge. Maximum shear stresses were calculated from the extrapolated data and also from the directly observable fringe orders at the apparent edges in the photographs. Both of these are given in Fig. 16 as a function of  $d/h$  ratio. Although the extrapolated stresses of this figure seem to indicate a slight tendency for the stress concentration to increase with  $d/h$  ratio, the scatter of the points is too great for any conclusions to be made. The absolute magnitude of these stress levels should not be regarded as generally applicable to other materials since there was most certainly a local inelasticity at these points.

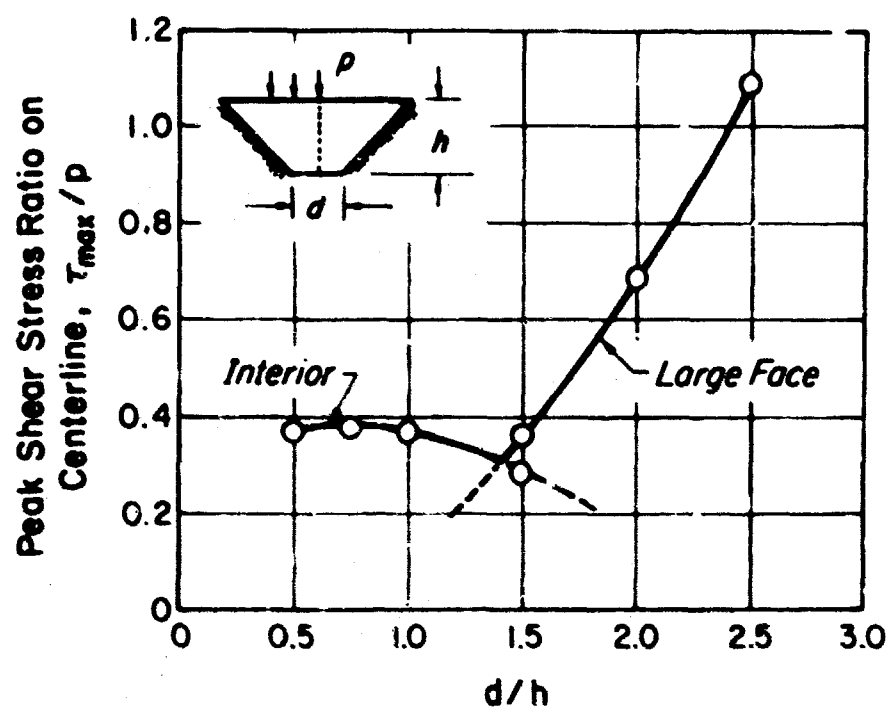


Figure 14 Peak shear stress on centerline as a function of  $d/h$  ratio.



Figure 15 Enlargement of a fringe concentration on the side near the edge of the small face (Model No. 9).

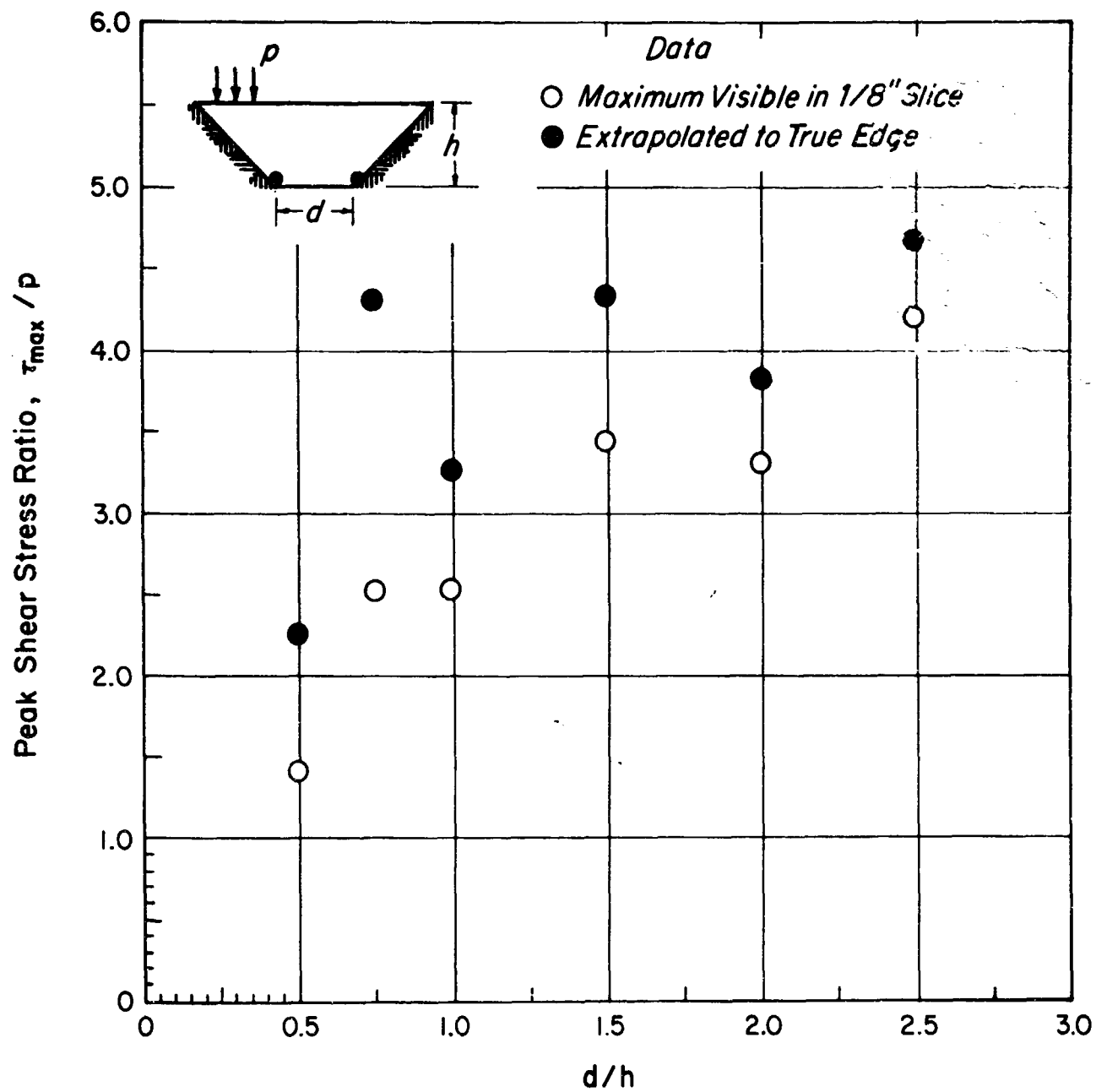


Figure 16 Measurements of the stress concentration near the edges of the small face as a function of  $d/h$  ratio.

## 6. Normal Stresses on Centerline

The radial stresses at the centers of the large and small faces of the six models were calculated using Eq. (1), and are plotted in Fig. 17. For  $d/h$  less than 1.0, the large face was in compression and the small surface was essentially stress free. With higher  $d/h$  ratios, the compression on the large face increased while the small face stress became tension at an increasing rate indicating the growing influence of a plate bending behavior as the windows became thinner.

The principal stresses along the centerline were calculated from the isochromatic and isoclinic fringe data for the two models having  $d/h$  values of 0.75 and 1.5. The stresses  $\sigma_r$  and  $\sigma_z$  were determined from Eqs. (5) and (6) and are plotted in Figs. 18 and 19. In both cases the axial stress  $\sigma_z$  decreased smoothly from the loaded to the unloaded faces. The radial stress  $\sigma_r$ , for  $d/h = 0.75$  in Fig. 18, shows a local rise in value towards the small face  $z = h$ , before dropping rapidly to zero. For  $d/h = 1.5$ , in Fig. 19, the radial stress became more linear as plate behavior played an increased role. In both cases, the maximum tensile and compressive stresses were developed on the boundaries.

The precision of these calculations depends on the accuracy of the fringe and isoclinic data. The isoclinics are not as sharp as the fringes and are difficult to locate precisely. Therefore, the curves of Figs. 18 and 19 have an uncertainty estimated at 5 to 10%.

## 7. Seat Angle Mismatch

None of the models had seat angles that exactly matched the corresponding angle of the seat fixture before the pressure was applied. The influence of the deformations induced in the models before full seating contact took place must therefore be examined.

The seat angle of each model was calculated from the measured dimensions and compared with the corresponding angle as measured on the seat fixture. These angles are included in Table 1. A positive mismatch angle is defined for a window making initial contact with the seat near the small face with a gap at the large face.

The range of mismatch angles for these models was  $\pm 8$  minutes of arc. The maximum gaps between the window and the seat are also included in Table 1. The effect of a gap at the small face of a model would tend to lessen the local contact forces near that face (a helpful condition) and to increase the magnitude of the plate bending behavior. The tendencies would be the opposite for a gap at

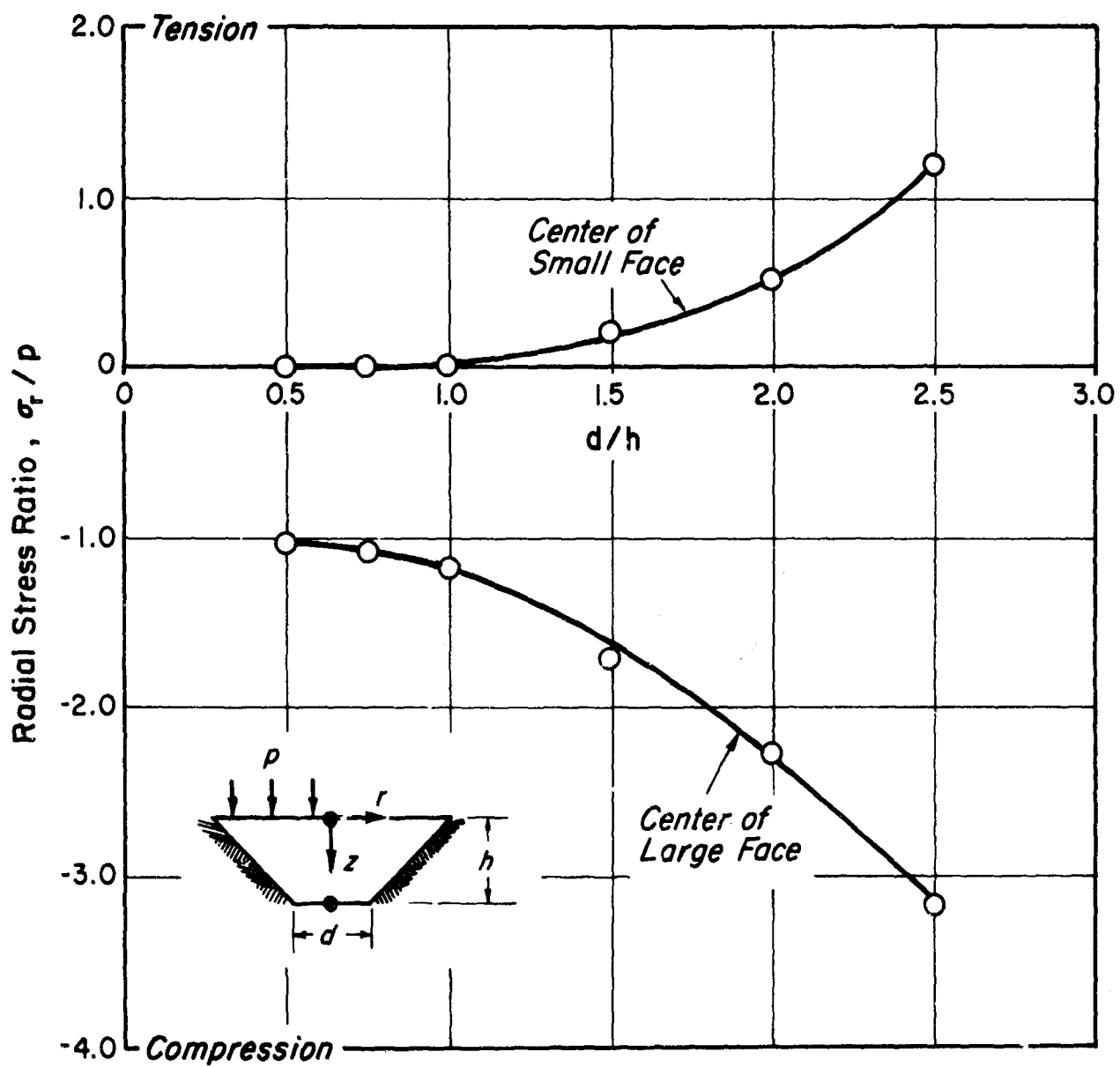


Figure 17 Radial stresses at center of large and small faces as a function of  $d/h$  ratio.

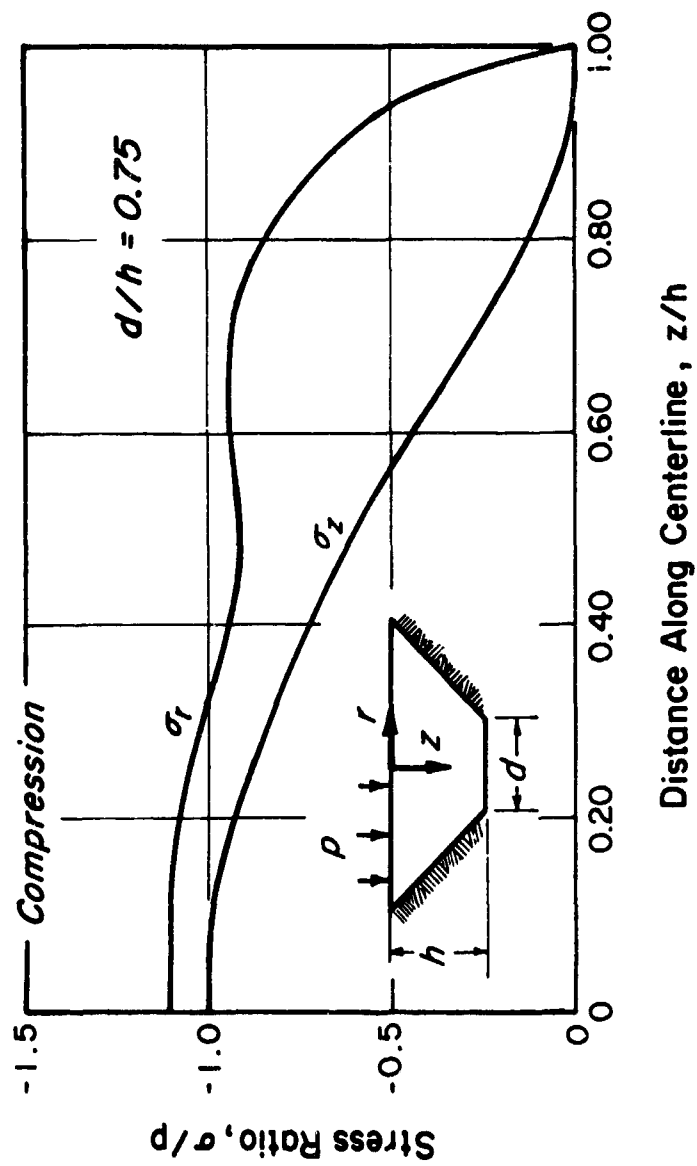


Figure 18 Principal stresses along the centerline of Model No. 4 with  $d/h = 0.75$  ( $\sigma_r = \sigma_\theta$ ,  $\tau_{rz} = 0$ ).

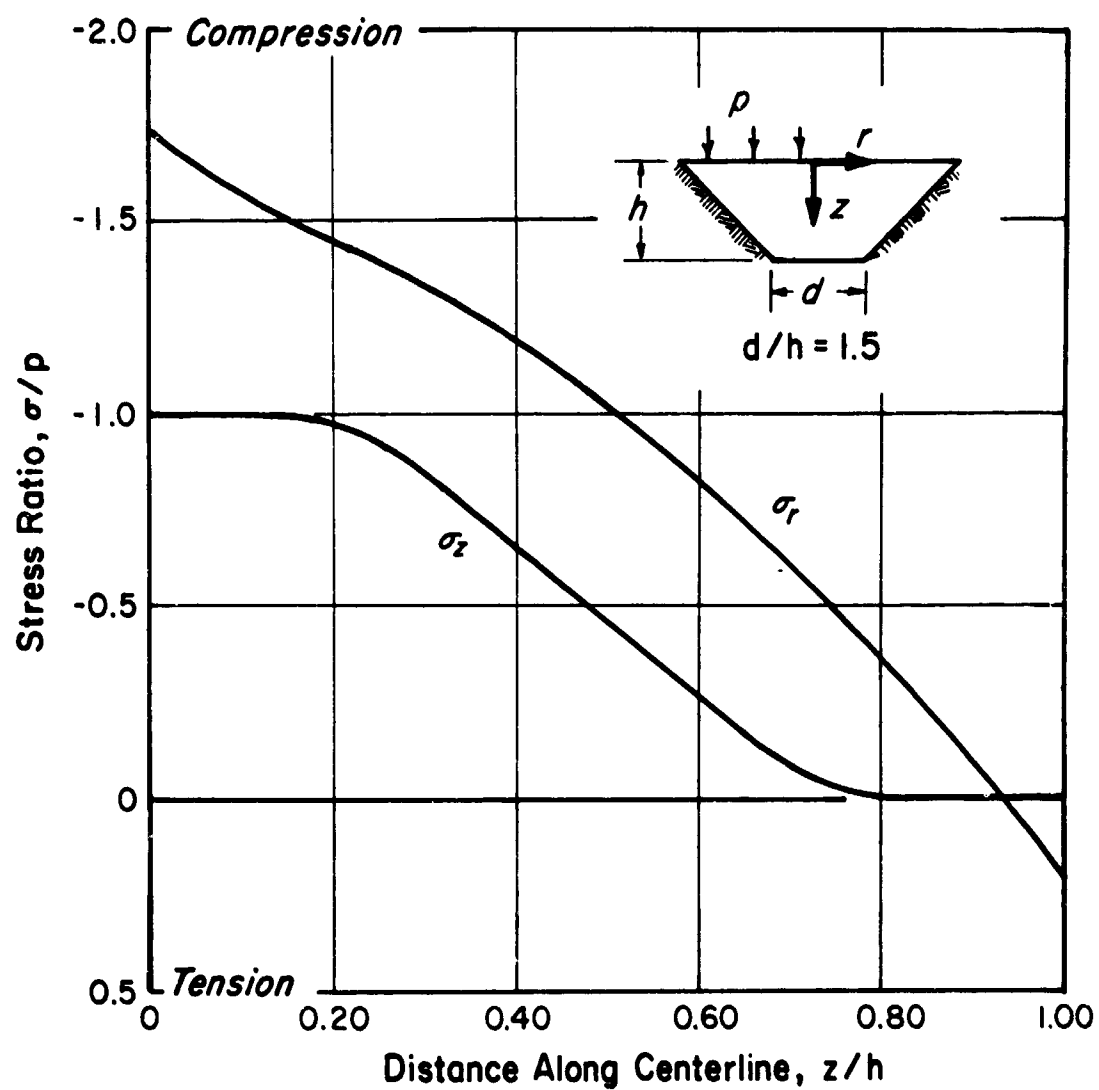


Figure 19 Principal stresses along centerline of Model No. 6 with  $d/h = 1.5$  ( $\sigma_r = \sigma_\theta$ ,  $\tau_{rz} = 0$ ).



the large end. This gap effect, if present, would be expected to diminish for larger  $d/h$  because of the increased flexibility of the thinner windows. Examination of Figs. 16 and 17 shows that these stresses do not exhibit such tendencies consistent with the values of seat gap given in Table 1.

The small mismatch angles therefore do not appear to have had an important effect on the behavior of models 3 through 8.

### C. Modified Windows

#### 1. Introduction

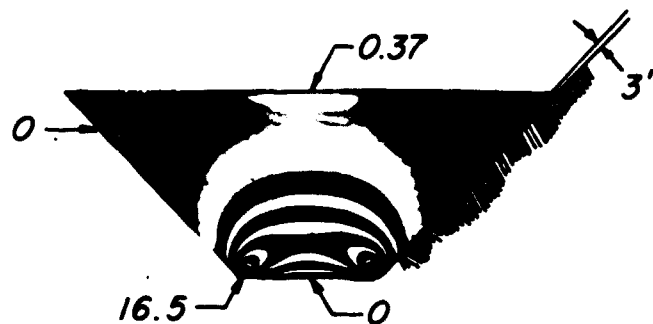
Two models with  $d/h = 0.75$  (which is in the range of current window designs) were stress frozen to examine the effects of certain geometrical modifications. One model had a spherical surface at the small end to check the hollow sphere theory and the other had a large gap at the small face to explore a way to reduce the local stress concentration on the cone near the small face.

#### 2. Spherical Small Face

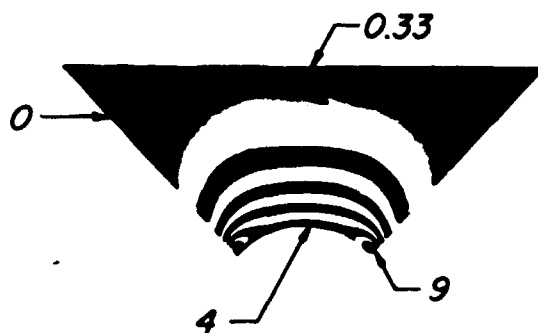
The data in Fig. 13 provide evidence that the conical windows in the range  $d/h \leq 1.0$  behaved fundamentally as conical sectors of a hollow sphere with a local influence of the flat small face geometry. In order to examine this assertion model no. 9 ( $d/h = 0.75$ ) was made with a spherical inner face of radius  $a = \sqrt{2} d/2$ , as in Fig. 3, so that the model was a segment of a hollow sphere except for the flat outer face. The fringe pattern and isoclinics are compared with those of the original model with  $d/h = 0.75$  (no. 4) in Figs. 20 and 21.

Examination of these figures shows that the fringes and isoclinics were only slightly affected by the removal of the lens-shaped piece. The hydrostatically stressed region remained as in the original model with  $d/h = 0.75$ . The portion of the conical surface under shear stresses was unchanged from the original model, as indicated by the  $45^\circ$  isoclinics of Figs. 21a and b. The differences in fringe pattern were restricted to regions close to the spherical surface, so that the presence of the flat surface causes only local changes.

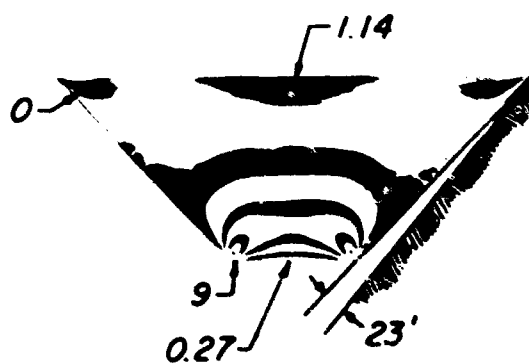
In Fig. 22, fringe order data along the centerline of this spherically faced model is compared to the prediction of the hollow sphere theory of Eq. (8). As before, the theoretical outer radius was taken as  $b = h + d/2$  as in Fig. 3, and the inner radius  $a = \sqrt{2} d/2$  was at the modified surface. The data for the original flat faced model with the same  $d/h$  ratio is reproduced here from Fig. 13 for comparison.



a.) Original Model with Gap at Large Face

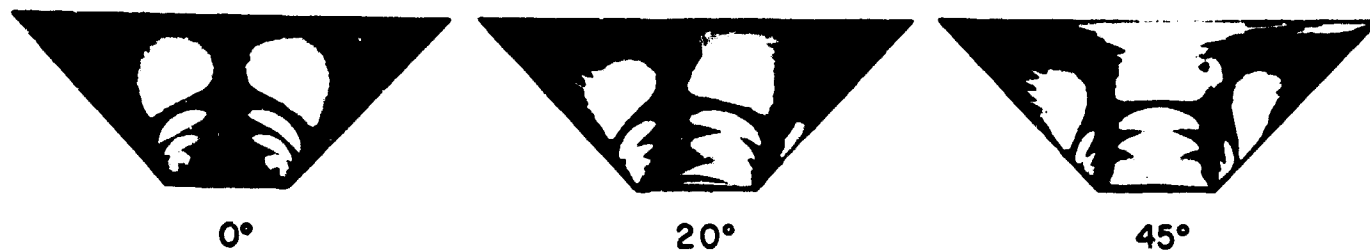


b.) Modified Model with Spherical Small Face

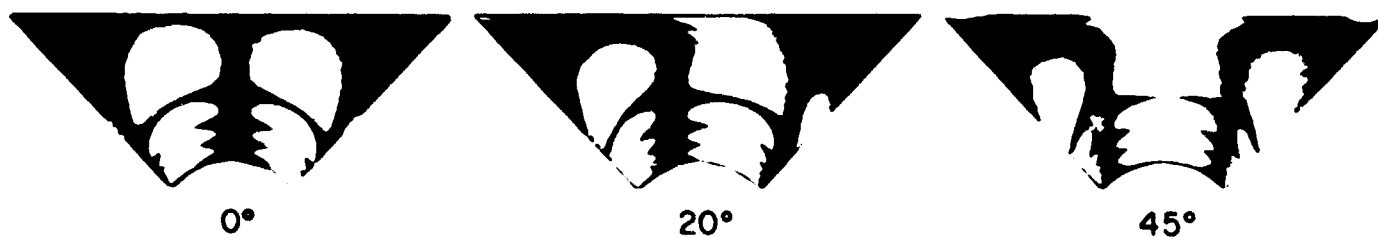


c.) Modified Model with Gap at Small Face

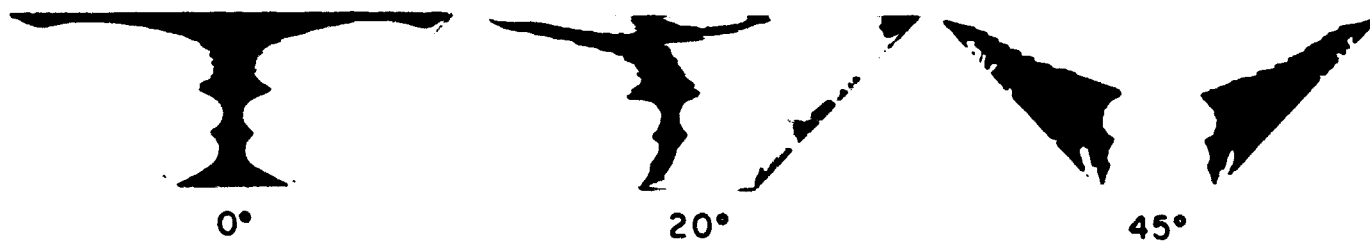
**Figure 20** Dark field fringe patterns of modified models compared to that of original design ( $d/h = 0.75$ ).



a) Original Model with Small Gap at Large Face



b) Modified Model with Spherical Small Face



c) Modified Model with Moderate Gap at Small Face

Figure 21  $0^\circ$ ,  $20^\circ$ , and  $45^\circ$  isoclinics of modified models compared to those of the original design.

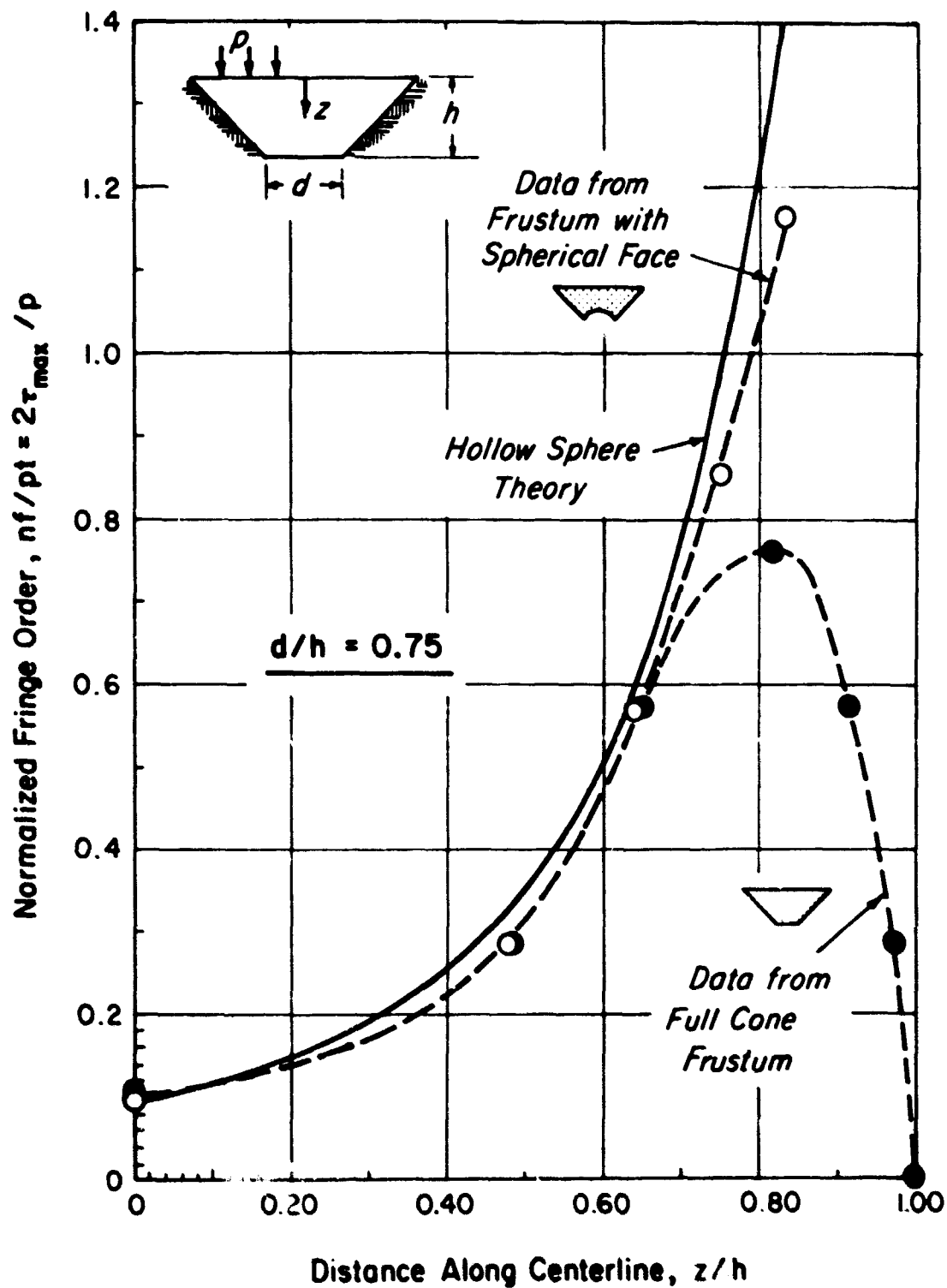


Figure 22 Comparison of fringe data on centerline with prediction of hollow sphere theory ( $d/h = 0.75$ ).

First note that in Fig. 22, the data from the spherically faced model and the flat faced model have the same good agreement to the hollow sphere theory until  $z/h = 0.65$ . After this point the flat-faced window data differ drastically from the theory, but the modified window data continue to follow the theory up to the spherical boundary where the difference between experiment and theory can perhaps be attributed to the effects of local friction on the conical surface near the small face. Friction would not be present in a segment of a homogeneous sphere.

This seems to support the hypothesis that the windows with  $d/h \leq 1.0$  behave basically as if they were conical segments acting within a complete hollow sphere under external pressure. Superimposed on this would be the interaction between the sphere segment and the lens shaped piece containing the flat small face, with the addition of friction effects.

The removal of the lens shaped piece caused one other notable change. The stresses in Table 2 and the fringe pattern of Fig. 20 show that the high local stress concentration of the original model was reduced about 65%. The explanation for this may be the reduction of the local stiffness under the concentrated contact forces by removal of the plano-convex lens.

The peak shear stress along the centerline occurred at the spherical surface and was increased by about 50% over the flat faced model (Fig. 22 and Table 2). The radial stress in the small face is given in Table 2 and was changed from zero in the original model to a moderately high compression, in the spherically faced model. The implication in this last result is that the tensile stresses in the flat small face of the windows with  $d/h > 1.0$  may be reduced or changed to compression by cutting a spherical surface.

### 3. Modified Seat Angle

The previous analysis of the possible effects of seat angle mismatch (Section B7) leads naturally to the possibility that a large negative mismatch angle with a gap at the small face of the window could reduce the contact forces at that end and thereby reduce the local stress concentration. Model No. 10, ( $d/h = 0.75$ ) was made with a negative mismatch angle of 23 minutes of arc, causing a moderately large gap at the sides near the small face. The fringes and isoclinics of this model, stress frozen under 40 psig, appear in Figs. 20c and 21c in comparison to those of the original model No. 4 for which the mismatch angle was +3 minutes.

Table 2

Stresses for Three Models with Nominal  $d/h = 0.75$

Model No.	Characteristic	$\sigma_r/p$ at small face center <sup>a</sup>	$\sigma_r/p$ large face center <sup>a</sup>	Peak $\tau_{max}/p$ on centerline	Extrapolated $\tau_{max}/p$ at concentration
4	original	0	-1.11	0.381	4.32
9	spherical small face	-1.17	-1.09	0.583	1.48
10	modified seat angle	-0.073	-1.31	0.308	1.71

<sup>a</sup>Negative values indicate compression

It can be seen by comparing Figs. 20a and 20c that the fringes were more widely distributed throughout this modified model and that the hydrostatic region at the upper corners almost disappeared. The  $45^\circ$  isoclinic appeared along most of the conical surface in Fig. 21c, except at the upper and lower edges, indicating that the friction shear stresses were confined to these two narrow areas near the faces.

The calculated stresses from this model are compared with that of the original model in Table 2. The maximum shear stress at the concentration was reduced about 60% by the use of this negative mismatch. Evidently the gap diminished the interference between the window and the seat and thereby reduced the local contact force at the edge of the small face. Although the stress in the small face was compressive for this model, it seems likely that this technique could induce tensile stress there when used on models with larger  $d/h$  because of the greater plate bending.

#### D. Effect of Pressure Level

Two models having  $d/h = 0.5$  were tested at pressures of zero and 10 psig to establish a basis for the data and to discover any influence of pressure level on the response.

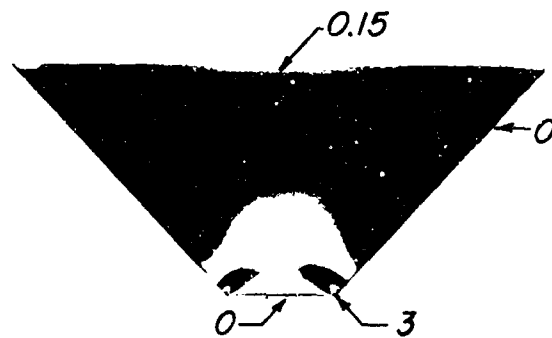
Window model No. 1, (no pressure applied) was a control. The fringe pattern appears in Fig. 22a. The nearly uniform very low fringe order throughout the slice verified that no significant stresses were induced by the experimental procedure.

For model No. 2 (frozen under 10 psig) the fringe pattern and isoclinics are compared to those of the 40 psig model (No. 3) in Figs. 23 and 24, which show that the general character of the internal stress distribution was the same under the two pressure levels. Stresses in these two models are given in Table 3. The data indicate that the magnitude of the internal stresses was approximately proportional to the applied pressure at least up to 40 psig, for this  $d/h$  ratio.

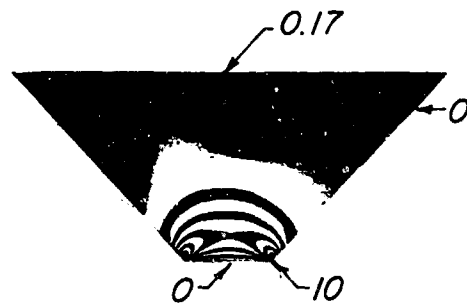
The region of hydrostatic stress was slightly smaller under the lower pressure, and the stress concentration extrapolated to the edge of the small face was slightly lower at the higher pressure, probably because of plasticity. Otherwise the character of the fringe patterns was the same for the two pressure levels.



a)  $p = 0$



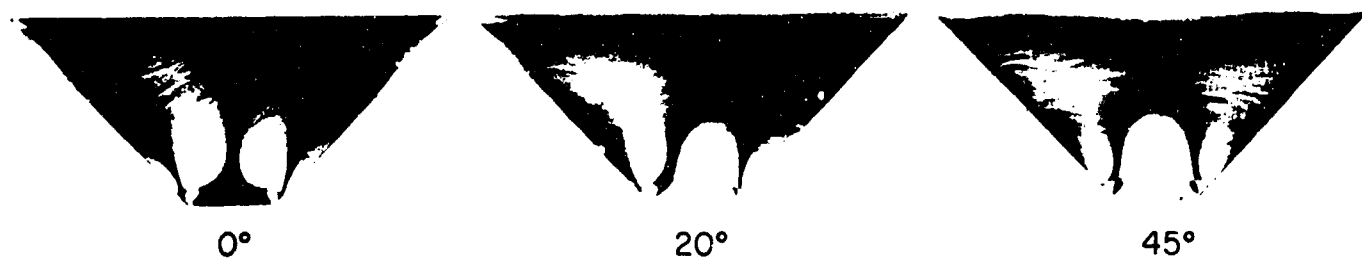
b)  $p = 10$  PSIG



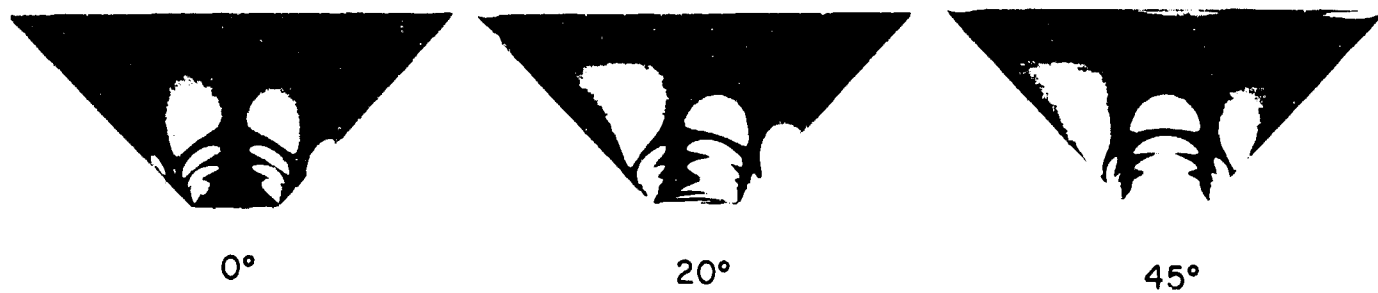
c)  $p = 40$  PSIG

Figure 23 Dark field fringe patterns from models with  $d/h = 0.50$  under different pressure levels.





a)  $p = 10$  psig



b)  $p = 40$  psig

Figure 24  $0^\circ$ ,  $20^\circ$ , and  $45^\circ$  isoclinics from models with  $d/h = 0.50$  under different pressure levels.

Table 3  
Effect of Variation of Applied Pressure  
d/h = 0.50

Model No.	p applied pressure psig	$\sigma_r/p$ large face center <sup>a</sup>	$\sigma_r/p$ small face center	$\tau_{\max}/p$ on center- line	extrapolated $\tau_{\max}/p$ at concentration
2	10	-1.045	0	0.370	2.37
3	40	-1.159	0	0.375	2.25

<sup>a</sup>Negative values indicate compression

## V. CONCLUSIONS

Considering the previous state of information on the subject, the results of this study represent an important contribution to the understanding of the structural behavior of deep submergence windows, and should be a significant step toward the development of improved window designs.

The data obtained revealed the important features of elastic stress fields of deep submergence windows in the range  $0.5 < d/h < 2.5$ , and have also indicated some promising techniques for improving the basic design. In the range  $0.5 < d/h < 1.0$ , the windows act as conical plugs and for  $1.0 < d/h < 2.5$ , the transition to plate behavior takes place.

The present data indicate that an appropriate model for visualizing the internal structural behavior of the windows in the range  $d/h < 1$  is a segment of an externally pressurized hollow sphere interacting locally with a plano-convex lens containing the flat small face as in Fig. 25. The flatness of the large face appears to be of little importance in this  $d/h$  range, since the stress field is nearly uniformly hydrostatic in its vicinity. For  $d/h > 1.5$  this simple model no longer applies as the plate bending behavior becomes important in the center region. Friction forces along the sides also have a moderate influence on the behavior near the small face.

It is common in the behavior of homogeneous, isotropic, and elastic bodies of simple geometry that the stresses are dependent only on the shape and the loading conditions and not upon the absolute size or the elastic modulus. Consequently, in the absence of contradictory data, the conclusions regarding the behaviors of the models should be valid for the full scale windows.

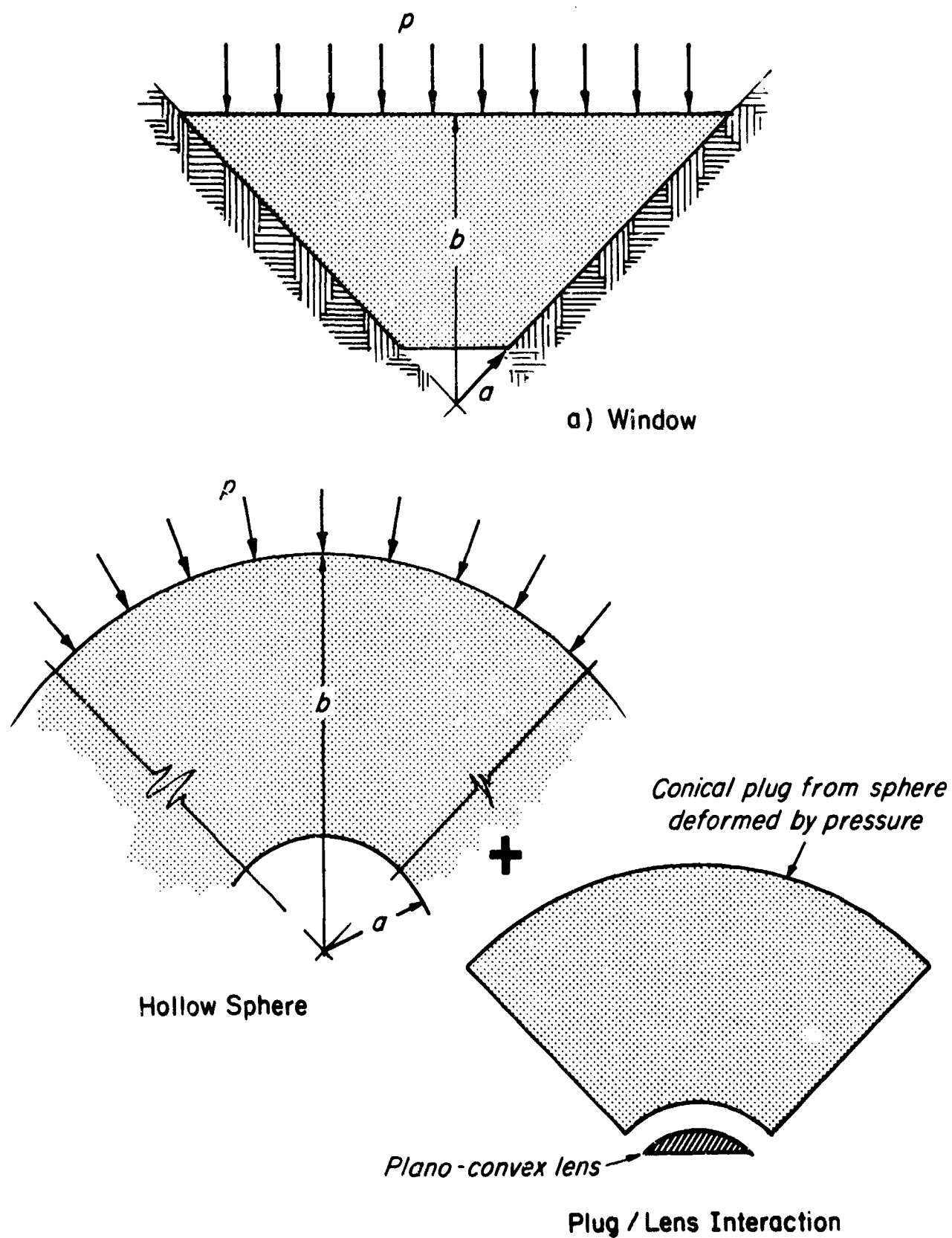


Figure 25 Components of window structural behavior for  $d/h \leq 1.0$ .

## VI. RECOMMENDATIONS

### A. Introduction

The information obtained in this study should provide a basis for the understanding of the structural failure of present window designs in the range  $0.5 < d/h < 2.5$ , and a starting point for improving the design. There are still many important aspects of the design problem to be explored. Knowledge of the dependence of the internal stresses and strength on such factors as slight shape modifications, seat angle, and load duration and cycling is essential for efficient and safe design of the window and seat structure combination. The recommendations that follow represent a course of action needed to obtain that knowledge.

### B. Improved Designs

The two geometrical modifications examined have shown a potential for improving the strength of the windows and should be explored further. The use of a spherical inner surface and also of a negative mismatch angle should be studied over a range of  $d/h$  values. Several variations of gap width along the seating surface should be examined as a refined strengthening device.

### C. Long Duration and Cyclic Loadings

Windows in operational deep submergence vehicles will generally be subjected to repeated cycles of pressure loading, each of many hours duration. It is important therefore to establish the dependence of Plexiglas window failure on load duration and number of cycles, and to examine failure not only with respect to short time strength data, but also in terms of the fatigue and creep properties of the Plexiglas at the operating temperature. Windows should be tested with load durations in the range of 1 hour to several days.

### D. Seat Angle

All the models examined here had a  $45^\circ$  seat angle, conforming with current design practice. The data indicate that a different seat angle could produce a lower stress level and a stronger window. This point should be clarified by a study of window stresses and strength in models with seat angles from  $30^\circ$  to  $60^\circ$  for several values of  $d/h$ .

## VII. REFERENCES

1. Piccard, A., "Earth, Sky, and Sea", Oxford University Press, N. Y., 1956 (Translation).
2. Hamilton, H., and H. Becker, "Photoelastic Investigation of Stresses in a Penetrated Hemisphere", Allied Research Associates, ARA-F-271-5, 21 December 1964.
3. Hamilton, H. and H. Becker, "Photoelastic Investigation of Stresses at Windows and Hatches in Spherical Pressure Vessels", Allied Research Associates, ARA-F-9250-3, 5 December 1963.
4. Frocht, M. M., "Photoelasticity", Vol. 1, Wiley, N. Y., 1941.
5. Timoshenko, S., and J. N. Goodier, "Theory of Elasticity", Second Ed., McGraw-Hill, N. Y., 1951.